A fundamental parameters approach to calibration of the Mars Exploration Rover Alpha Particle X-ray Spectrometer

J. L. Campbell,[1] M. Lee,[1] B. N. Jones,[1,2] S. M. Andrushenko,[1] N. G. Holmes,[1] J. A. Maxwell,[1] and S. M. Taylor[1]

Received 29 September 2008; revised 8 January 2009; accepted 13 February 2009; published 15 April 2009.

[1] The detection sensitivities of the Alpha Particle X-ray Spectrometer (APXS) instruments on the Mars Exploration Rovers for a wide range of elements were experimentally determined in 2002 using spectra of geochemical reference materials. A flight spare instrument was similarly calibrated, and the calibration exercise was then continued for this unit with an extended set of geochemical reference materials together with pure elements and simple chemical compounds. The flight spare instrument data are examined in detail here using a newly developed fundamental parameters approach which takes precise account of all the physics inherent in the two X-ray generation techniques involved, namely, X-ray fluorescence and particle-induced X-ray emission. The objectives are to characterize the instrument as fully as possible, to test this new approach, and to determine the accuracy of calibration for major, minor, and trace elements. For some of the lightest elements the resulting calibration exhibits a dependence upon the mineral assemblage of the geological reference material; explanations are suggested for these observations. The results will assist in designing the overall calibration approach for the APXS on the Mars Science Laboratory mission.

Citation: Campbell, J. L., M. Lee, B. N. Jones, S. M. Andrushenko, N. G. Holmes, J. A. Maxwell, and S. M. Taylor (2009), A fundamental parameters approach to calibration of the Mars Exploration Rover Alpha Particle X-ray Spectrometer, *J. Geophys. Res.*, *114*, E04006, doi:10.1029/2008JE003272.

1. Introduction

[2] The Alpha Particle X-ray Spectrometer (APXS) has established itself as a powerful instrument for quantitative elemental analysis of planetary surfaces. The APXS on the Mars Pathfinder mission [*Rieder et al.*, 1997] analyzed 12 rock and soil samples using alpha particles and X-radiation to induce characteristic X-ray emission, and using the alpha particles in parallel for Rutherford Backscattering Spectroscopy (RBS), which is sensitive to very light elements such as carbon and oxygen that are not accessible via X-ray spectroscopy. For the Mars Exploration Rover (MER) mission, significant improvements were made to the X-ray emission analysis capabilities, partly at the expense of the detection sensitivity of the RBS mode [*Rieder et al.*, 2003]. Over 400 Martian rocks and soils have now been subjected to elemental analysis by the APXS units on board the Spirit and Opportunity rovers [*Brückner et al.*, 2008]. As shown schematically in Figure 1, each MER APXS carries six ^{244}Cm radionuclide sources arranged in an annulus which surrounds a collimated silicon drift X-ray detector (SDD). The device thus provides two quite different X-ray emission analysis methods which operate simultaneously: X-ray fluorescence analysis (XRF) is accomplished using the plutonium L X rays emitted by the source, while particle-induced X-ray emission analysis (PIXE) is accomplished with the 5.806 MeV alpha particles.

[3] An improved APXS design has been developed (R. Gellert, private communication, 2008) for the Mars Science Laboratory (MSL) mission, providing some three times greater rate of data accumulation and hence promising lower element detection limits in a given time as compared to the MER devices.

[4] The increasing sophistication of the APXS instrument merits a concomitant effort to improve the sophistication of the calibration procedure upon which APXS analytical data are based. The upcoming MSL mission renders such an effort timely. In this paper we describe a ''fundamental parameters'' approach to the treatment of the APXS spectra. Our work resulted directly from a suggestion (R. Rieder, private communication, 2003) by the Principal Investigator of the MER APXS team. His proposal was that it should be possible to augment the GUPIX spectrum treatment software [*Maxwell et al.*, 1995] that is widely used in accelerator-based PIXE analysis with an analogous XRF treatment, and then to merge these codes to cope with spectra that arise from two different X-ray excitation mechanisms that are deployed simultaneously upon a single sample.

[5] The calibration philosophy and procedure adopted for the two MER flight instruments and a laboratory spare instrument, each with its own set of ^{244}Cm sources, were described in detail by *Gellert et al.* [2006]. Spectra were

[1]Guelph-Waterloo Physics Institute, University of Guelph, Guelph, Ontario, Canada.
[2]Now at Surrey Ion Beam Centre, University of Surrey, Guildford, U.K.

0148-0227/09/2008JE003272

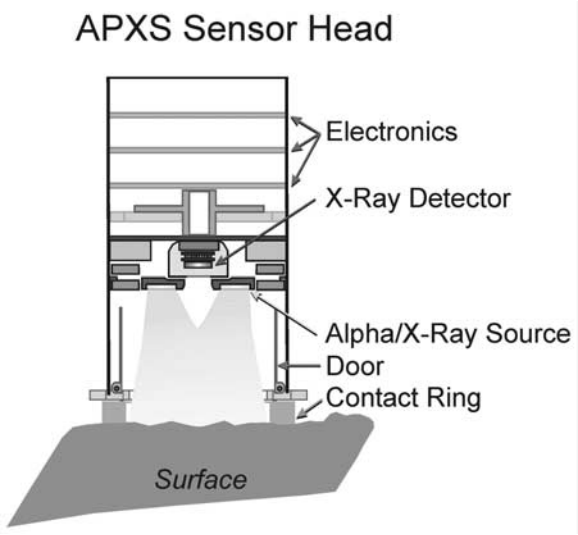

Figure 1. Schematic of the Alpha Particle X-ray Spectrometer (APXS; reprinted from *Gellert et al.* [2006]).

recorded on each instrument in a ''cross-calibration'' exercise using a set of eleven geochemical reference materials. The relatively small size of this suite of materials presumably reflected the limited duration of the calibration period that was possible within the MER mission schedule. The spare instrument calibration was extended with a larger set of geochemical reference materials together with a set of pure elements and simple chemical compounds, thereby providing a significant extension of the types of materials studied. These data enabled Gellert et al. to refine the calibration of the two flight instruments, whose results exhibited small differences reflecting differences in quantities such as source activity and detector window thickness. It is the larger set of spectra from the spare instrument calibration, not published elsewhere but made available to us, that we employ here.

[6] Spectrum analysis in the *Gellert et al.* [2006] cross-calibration exercise employed a dedicated peak-fitting program which provided the areas of the principal characteristic X-ray peak for each element in each sample. Next, a matrix correction was applied post facto to account for attenuation effects within each (infinitely thick) sample. Then, for a given APXS, the sensitivity for each element, i.e., the ratio between X-ray counts and concentration was determined for an ''average'' matrix. This sensitivity relationship could then be used for spectra of unknown samples, with the matrix correction applied to compensate for the difference between that sample and the average of the reference materials.

[7] One merit of a fundamental parameter approach, as developed here, is that matrix effects are built in rigorously from the outset and are used in both the spectrum fitting and the conversion of peak areas to concentrations. Thus, for example, the Kβ/Kα X-ray intensity ratio for each element is adjusted for matrix effects within the fitting process. The physics outlined in section 2 provides different matrix corrections for the PIXE and XRF components of the X rays of each element, and these are rigorously computed in the appropriate ratio. The code that we have developed is named GUAPX. Our first objective here is to ascertain to what degree the response of the APXS instrument can be understood in terms of the fundamental physics of the X-ray excitation processes and the detector physics. The second objective is to test this approach for major, minor and trace elements. The third is to probe for possible dependences of the resulting calibration upon the specific nature of the geological reference materials used. The work is accomplished using the extended set of flight spare instrument spectra mentioned above. A subsequent paper will apply the new GUAPX approach to selected APXS spectra from Spirit and Opportunity.

[8] The XRF method is widely employed for terrestrial whole rock analysis, but it is important here to recall that for major element determination the sample is invariably subjected first to lithium borate fusion to eliminate mineral phase heterogeneities [*Potts*, 1987]; in contrast, trace elements are routinely determined in compressed powder pellets. It is well known that in the absence of the fusion step, large errors can arise. PIXE is not widely employed for whole rock work (its strength lies in trace element analysis and mapping of individual grains with micron spatial resolution [*Campbell and Czamanske*, 1998], but the same remarks hold. Obviously, however, sample fusion and microbeam analysis are presently precluded on Mars, and so important aspects of the present work are to assess the limits placed upon the analytical accuracy of the APXS by the mineralogical phase heterogeneity of rock samples and to consider possible means of overcoming these limits.

2. Physics of the APXS

[9] In the APXS, X rays of the light elements (Na, Mg, Al,...) are excited almost exclusively by PIXE via the helium ions from the ^{244}Cm sources. Characteristic X rays of elements lighter than these (C, O,..) need not be considered because of their large absorption in the detector window and in the Martian atmosphere (6–10 mbar CO_2). The X rays of the heavier elements observed (Fe-Zr) are excited almost exclusively by XRF. At approximately Z = 21, the two excitation processes contribute equally to the observed X-ray intensities.

[10] In both the PIXE and XRF methods, the yield $Y(Z)$ of characteristic X rays of element Z, produced by a number N of monoenergetic ions or monoenergetic photons incident on the infinitely thick sample, is given by the same form of relationship:

$$Y(Z) = Y_1(Z, M) N \, C_Z \, \Omega \, t_Z \, \varepsilon_Z \qquad (1)$$

The symbol 'M' indicates that the X-ray yield depends not only upon the concentration C_Z of the specific element of interest but also upon those of all the other elements that define the sample matrix through their influence upon the incoming and outgoing radiations. Detailed derivations and discussions of this relationship are found in many references, examples being *Van Grieken and Markowicz* [2002] for XRF and *Maxwell et al.* [1995] for PIXE. $Y_1(Z, M)$ is the theoretical X-ray yield from element Z per unit concentration within a defined matrix M, per steradian of solid angle, per ion or photon; N is the number of incident monoenergetic ions or monoenergetic photons; Ω is the detector solid angle in steradians; t_Z is the transmission

Table 1. Analyzed Depths D_{90} and PIXE Contributions for the Basalt Reference Material BE-N[a]

Element	D_{90} (μm)	PIXE fraction (%)
Na	2.6	100
Mg	3.8	100
Al	5.2	100
Si	6.1	100
P	4.4	100
S	5.4	99.7
Cl	6.1	99.4
K	7.6	97.4
Ca	8.2	94.8
Ti	18.2	76.2
Mn	68.7	20.2
Fe	89.3	10.9
Zn	187	0.9

[a]PIXE, Particle-Induced X-ray Emission.

through any material between the detector and the sample; ε_Z is the intrinsic efficiency of the detector, including the attenuating effects of the beryllium window, the nitrogen filling and the aluminum contact.

[11] Equation (1) cannot be used directly to deduce C_Z from the measured value of $Y(Z)$, because the term $Y_1(Z, M)$ contains the C_Z values for all elements present, whether they are represented by X rays in the spectrum or not. This ''matrix term'' describes the attenuation in the sample matrix of incoming or outgoing photons and the slowing down of incoming ions. In the GUAPX code these effects are computed from an extensive database of ionization cross sections, photoelectric cross sections, helium ion stopping powers, and X-ray attenuation coefficients. In PIXE, the X-ray production decreases with depth because the ions slow down and therefore the ionization cross section decreases. In XRF there is also a decrease in X-ray production with depth, but in this case the reason is that the number of exciting monoenergetic photons diminishes exponentially with depth in the sample. To compute $Y_1(Z, M)$ the code assumes that the elements are homogeneously distributed within the sample material.

[12] In the APXS, the number N is proportional to the measurement duration T, i.e., $N = aT$ where ''a'' is a constant. We can therefore draw the quantities a and Ω together into a single instrumental factor H. Equation (1) for either X-ray excitation method thus becomes

$$Y(Z) = Y_1(Z, M)\, T\, C_Z\, H\, t_Z\, \varepsilon_Z \tag{2}$$

Recognizing the need to sum over excitation produced by approximately twenty monoenergetic Pu L X-ray lines, we can now write the overall yield equation for the APXS as

$$Y(Z) = H\, C_Z\, T \left[Y_{1,\mathrm{PIXE}}(Z, M) + \sum Y_{1,\mathrm{XRF}}(Z, M) \right] t_Z\, \varepsilon_Z \tag{3}$$

The value of H can be determined by measurements upon standards and upon reference materials carried out in precise and reproducible geometry. The possibility of small systematic errors in the database or the detector description cannot be ignored, and so an element-dependent empirical correction factor k is introduced; one hopes that k will have value 1.0, but our long PIXE experience suggests that in practice it may differ slightly from 1.0 and have a slight dependence upon atomic number. Equation (3) thus becomes

$$Y(Z) = H\, C_Z\, T\, k(Z) \left[Y_{1,\mathrm{PIXE}}(Z, M) + \sum Y_{1,\mathrm{XRF}}(Z, M) \right] t_Z\, \varepsilon_Z \tag{4}$$

[13] Since PIXE and XRF are usually conducted with geometrically well-defined beams of exciting radiation, equation (1) is customarily evaluated at unique values for these angles, relative to the sample surface, of the incoming radiation and the outgoing characteristic X rays en route to the detector. For the source-excited situation in the APXS, the geometry (see Figure 1) is very different, as discussed by *Omand et al.* [2005]. There is a wide range of directions for the incident ions and photons, and, as a consequence of that, there is also a wide range of directions for the excited characteristic X rays. Omand et al. showed via Monte Carlo calculations of X-ray yields that a pair of ''effective angles'' could be defined such that equation (1), evaluated with these two angle values, provides the same X-ray yields as the Monte Carlo approach which properly treats the full ranges of angles.

[14] Obviously, GUAPX demands an accurate value for the intensity ratio between L X rays and alpha particles emitted by ^{244}Cm in order that the proper relative contributions from the two excitation modes are established; the most recent measurement [*Johnston and Burns*, 1995] of this quantity agrees within 1.5% with the value that is deduced from the ^{244}Cm decay scheme [*Firestone*, 1996] using recently published nuclear and atomic data [*Band et al.*, 2002; *Campbell*, 2003].

[15] Because X-ray generation by helium ions depends upon the ion energy, an accurate value for that energy is also required. The energy is reduced from the decay scheme value of 5.806 MeV by both finite source thickness and by passage through the titanium cover foils that protect the sample from being contaminated by plutonium ions recoiling out of the source. Here we take the energy as 5.135 MeV on the basis of actual helium ion energy spectra recorded by *Rieder et al.* [2003].

[16] The depth of sample that is ''interrogated'' differs in the two techniques; for either technique it varies among elements and depends upon the sample matrix. This depth dependence can be quantified through the quantity D_{90}, which is the depth (in microns) above which 90% of the detected X rays of a given element are generated. Values of D_{90} computed by GUAPX under the assumption of a homogeneous matrix are presented in Table 1 for the basalt reference material BE-N. Table 1 also shows the fraction of these X rays that arise from helium ion excitation (PIXE). It is clear that the depth of analysis for the light elements (PIXE) is very much smaller than that for the heavier elements (XRF).

3. Reference Materials

[17] The full set of materials employed to calibrate the sensitivity of the MER APXS included (1) various pure elements and simple chemical compounds; (2) geochemical reference materials (GRMs) issued by bodies such as the U.S. Geological Survey, the Japanese Geological Survey

Table 2. Geological Reference Materials Used in the Mars Exploration Rover Alpha Particle X-ray Spectrometer Calibration

GRM[a]	Supplier[b]	Supplier's Description
AC-E	SARM	Granite
AGV-1	USGS	Andesite
Al-I	SARM	Albite
AN-G	SARM	Anorthosite
BCR-1	USGS	Basalt
BE-N	SARM	Basalt
BR	SARM	Basalt
BX-N	SARM	Bauxite
DR-N	SARM	Diorite
DT-N	SARM	Kyanite
FK-N	SARM	Potash feldspar
GA	SARM	Granite
GH	SARM	Granite
GL-O	SARM	Glauconite
GS-N	SARM	Granite
GXR-1	USGS	Jasperoid
IF-G	SARM	Iron formation
JSD-2	JGS	Stream sediment
MAG-1	USGS	Marine sediment
MA-N	SARM	Granite
Mica-Fe	SARM	Biotite
Mica.Mg	SARM	Phlogopite
PM-S	SARM	Microgabbro
UB-N	SARM	Serpentine
VS-N	SARM	Aluminosilicate glass
WS-E	SARM	Dolerite

[a]Geological reference materials.
[b]SARM, Service d'Analyse des Roches et des Mineraux du CNRS; USGS, U.S. Geological Survey; JGS, Japanese Geological Survey.

and the French Service d'Analyze des Roches et des Mineraux (SARM) du CNRS; (3) in-house GRMs of the Max Planck Institűt fur Chemie (Mainz, Germany), which in turn included two terrestrial andesite rocks and several meteorite materials. It was decided here to employ only groups 1 and 2 in reaching quantitative conclusions.

[18] The chemical ''reference materials'' used here are restricted to pure elements, oxides, chlorides, sulfates and nitrates; one departure from this simplicity is a hydroxyapatite that was included by *Gellert et al.* [2006]. Most of these were fine powders, but a few were solid samples; more detail is given in section 7. The geological reference materials are listed in Table 2; they were supplied in powder form, having been sieved by the supplier to ensure a maximum particle size of 70–80 μm. The GRM suite contained thirteen igneous rocks, two sediments, seven essentially pure minerals, an artificial aluminosilicate glass, and three other materials that do not fall into one of the above groups. Two of the igneous GRMs that were used in the MER APXS calibration were excluded from the present work because no uncertainty estimates for the concentrations were provided by the supplier. The work that follows below will suggest the desirability of adding further geological reference materials in any future APXS calibration. But this avenue is not available to us in the present exercise, which is conducted with an inherited data set.

4. Measurement Details

[19] Only a few details are given here, because a full description of the MER APXS, together with extensive information about the measurements, is given by *Gellert et al.* [2006]. The silicon drift detector (SDD) within the APXS, manufactured by Ketek GmbH, had a 5 μm beryllium window and was fitted with a 3 mm diameter zirconium collimator. The internal 1.8 mm gap between window and detector crystal was filled with nitrogen at 1 bar pressure. The manufacturer's specifications did not provide information on any dead layer or layer of incomplete charge collection. The geometry of the arrangement is shown in Figure 1, and the distance between the window and the surface of each GRM sample was 32.7 mm. Prior to use, each powder sample was placed in a circular dish which more than filled the field of view of the device, and the surface was rendered as smooth as possible. The actual thickness of the samples is not known, but evidence that they were sufficiently thick emerged during our analysis of the data.

[20] The sample and the APXS, cooled to −40C to achieve energy resolution of ~160 eV (full width at half maximum) for the manganese Kα X-ray line, were located within a vacuum chamber. This permitted measurements to be taken both under vacuum and at 10 mbar pressure of carbon dioxide, the latter approximately emulating the Martian atmosphere. All the GRM data were taken at 10 mbar pressure of CO_2; about half of the chemical compound measurements were done in the CO_2 atmosphere and about half under vacuum.

5. Data Analysis Methodology for the GRMs

[21] Figure 2 displays a typical APXS spectrum, in this case from the basalt reference material BE-N. GUAPX takes the same approach to fitting such spectra as the GUPIX code from which it is derived [*Maxwell et al.*, 1995]. Each element is represented in the spectrum by several X-ray lines whose energies and relative intensities are stored in the database. The relative intensities are adjusted to reflect the influence of detector efficiency, any absorbing material between sample and detector, and the sample matrix composition. Each line is modeled as a Gaussian or Voigtian peak, with the height of only the most intense line of each element being a variable of the nonlinear least squares fit; all other lines of that element are held to the appropriate relative intensity. The relationship between peak centroid and X-ray energy is linear; that between peak width and X-ray energy is linear in terms of the square root of the latter. The four parameters of these two relationships are variables of the fits. The number of parameters varied is thus $N + 4$ where N is the number of elements present. Continuous background is removed by a digital filtering procedure within each iteration of the fit. For more intense peaks such as that of iron, a description of low-energy tailing is incorporated. Two standard ''recipes'' are available to describe pulse pileup. The treatment of the Rayleigh and Compton scatter peaks of the exciting Pu X rays is described by us elsewhere [*Mallett et al.*, 2006].

[22] Again as in the GUPIX case, GUAPX can run in two modes. In ''fixed matrix mode,'' the major and minor elements that comprise >99% of the matrix are presumed known together with their concentrations; the matrix terms are computed once from these, the spectrum fit is then iterated to minimum chi-square, and the concentrations of all elements whose X rays are in the spectrum are deduced via equation (4). An a priori value for the instrumental constant H is required. The elements thus determined

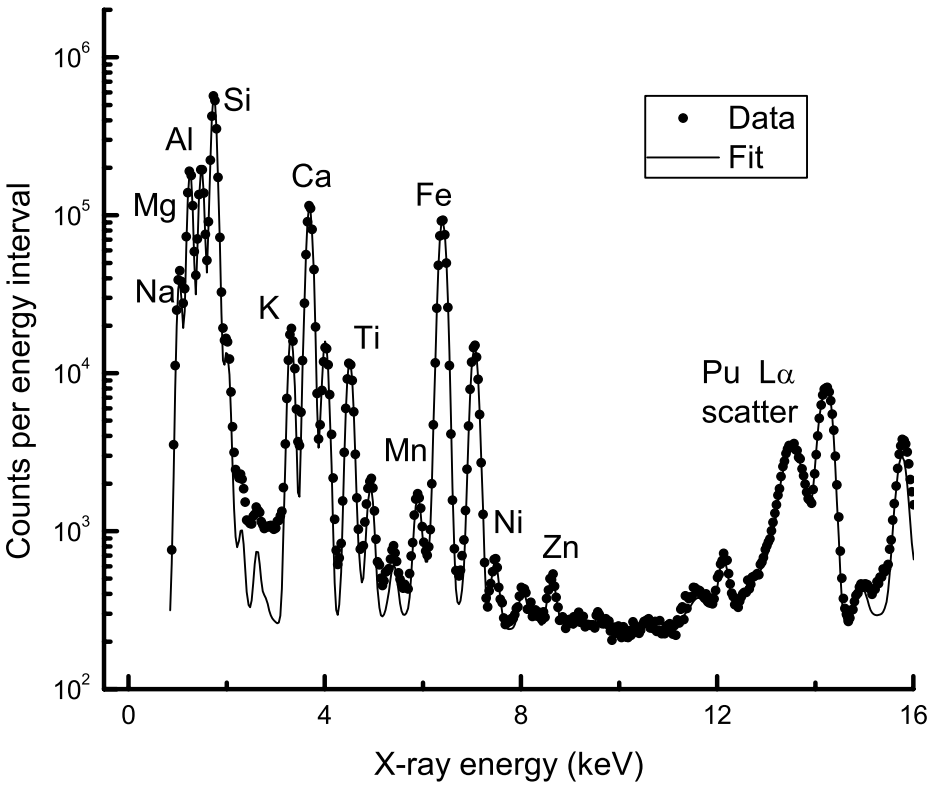

Figure 2. Typical APXS spectrum (Service d'Analyse des Roches et des Mineraux du CNRS basalt BE-N).

include both trace elements and the matrix (major and minor) elements, and a comparison of the fitted concentrations of the latter with known values provides a useful check on the accuracy of the code. In ''iterative matrix mode,'' nothing is presumed to be known ab initio, and all the element concentrations are iterated until the optimal solution is reached; within each iteration of the elemental content, which provides a new set of matrix corrections, there is a complete reoptimization of the least squares fit. This approach requires that all elements present are able to contribute their X rays to the spectrum. However, in the present application to geochemistry, where oxygen is present in the sample but invisible in the spectrum, the standard XRF geochemical approach is taken, wherein oxygen is coupled stoichiometrically to each ''visible'' element and thereby included in all the matrix calculations. The sum of the oxide concentrations is normalized to 100%, and therefore in this mode a value for the instrumental constant H is not required (although the Z-dependent quantity k is required). This is important on Mars, where the geometry and hence the H value vary from one sample to another: for the flight spare instrument calibration data used here, the geometry was, with a few noted exceptions, constant.

[23] In its final version the GUAPX code will be used in iterative matrix mode. However, at the present, exploratory stage of our work, we prefer not to use this approach, because it is important to avoid our results being skewed by the imposition of the 100% closure rule; *Rollinson* [1993] emphatically points out the pitfalls of such closure. If, for example, database or fitting weaknesses cause spuriously high concentrations for some elements, then the concentrations of others will be artificially depressed; it is then difficult to ascertain which are the original errors as opposed to the ensuing ones. Another reason is that bound water content can be included in the fixed matrix approach but not in the iterative mode, leading to erroneous results in the latter.

[24] Our approach is composed of three stages; in each stage we work in terms of the ratio R of an element's GUAPX concentration to the supplier's concentration value. We then derive for each element its error-weighted mean value R_{wm} across the subset of GRMs that contain detectable quantities of that element. If the reference material is homogeneous, we would expect that for each element, the R_{wm} value would be unity. The error weighting combines both the two standard deviation (or 95% confidence level, CL) uncertainty in concentration quoted in the supplier's documentation and the two standard deviation uncertainty in the concentration derived from the GUAPX fitting process. In any reference below to a mean value of R, this is to be taken as the mean calculated with full error weighting. An important advantage of adopting well-known and widely used GRMs is that estimates of the uncertainty values for their concentrations are provided, albeit with different degrees of rigor.

[25] In the first stage, the system H value is deduced from the 4 measurements of silicon in SiO and SiO_2 and the 25 measurements of silicon in the GRMs. There are advantageous aspects to the choice of silicon for determination of the system H value. The X rays of the four lightest elements (Na, Mg, Al, Si) are induced almost entirely by PIXE, whereas those of the heavier elements detected (Mn, Fe, Zn) are induced almost entirely by XRF. Thus any systematic

deviation of the R_{wm} values for the heaviest elements relative to that of silicon sheds light on the consistency of the cross sections for the two ionization mechanisms. In addition, any systematic Z dependence of the three lightest elements relative to silicon may reveal inaccuracies in the transmission factors of their low-energy X rays in APXS materials. There is a 0.2 mm uncertainty in the 1.8 mm value that is given by the manufacturer as the length of the nitrogen column within the detector; combining this with a pessimistic guess at a 10% uncertainty in the Be window thickness we find ± 2% uncertainty in the transmission of silicon K X rays through these two absorbers. The corresponding value for sodium is close to ±20%.

[26] The second stage involves an examination of the data from the simple chemical element and compound reference materials; issues of mineral phase inhomogeneity are not expected here. Any observed variations in R_{wm} for the various elements as a function of atomic number can then assist us both in probing database weaknesses and in determining unknown instrumental parameters.

[27] The third stage is an analysis of the geological reference materials. This work is expected to test the assumption of phase homogeneity in these geological materials and to indicate the level of accuracy afforded by the GUAPX approach.

[28] There is a negative aspect to our method in that it assumes that every specimen was placed at precisely the same distance from the APXS. That distance was about 35 mm, and so even a placement error of 0.35 mm for a given specimen would cause a 2% change in solid angle and hence in the derived R value for that case. This introduces a degree of scatter into the results and increases experimental uncertainties; however, the large number of materials employed offers a significant averaging and hence reduction of this effect.

[29] Our approach has similarities to that of *Gellert et al.* [2006], but there are important differences. The main similarities are the assumption of a homogeneous distribution of elements within the materials analyzed and the neglect of particle size effects. Our GUPIX code does offer limited possibilities to study layered samples, but this option does not yet exist in GUAPX; neither code attempts to attack the difficult issue of a sample that contains several distinct mineral phases, randomly distributed, each separately having uniform elemental distribution. Particle size effects have been studied in XRF since the early work of *Bernstein* [1962] and of *Claisse and Samson* [1962]. In the present work, the issue, somewhat simplified, is that the granularity of the sample surface may cause X rays emitted from one particle to interact with another particle, resulting in attenuation and enhancement effects. Computational modeling [*Campbell et al.*, 1985] of proton-induced X-ray yields from randomly rough surfaces of a homogenous material shows that roughness at the micron level will cause a decrease in characteristic X-ray yields. *Claisse and Samson* [1962] studied the more complex XRF case where the individual particles at the surface are of different mineral types. The experimental arrangement of the MER APXS has two advantages in terms of the particle size issue: first, the mean angles of incidence of both the exciting and the emitted radiation are close to the sample normal; second, the excitation depth D_{90} (see Table 1) for the 5 MeV helium ions is only a few microns. Together, these two facts suggest that the issue most likely to arise here is not one of different particles but of different mineral phases within one particle.

[30] The main difference between the two approaches is the incorporation here of fundamental parameters at the outset as opposed to the application of an approximate matrix correction after the spectrum fitting. *Gellert et al.* [2006] determine the "sensitivity" for each element by averaging over a large number of the combined group of reference materials, with sensitivity being defined as the X-ray counts per unit time per unit concentration for an "average matrix." Thus their description refers individually to each element rather than to the system overall; the sensitivity varies significantly from element to element and interpolation is required for elements not present in the reference materials. Our approach characterizes the system overall through the H value, and it is thus effectively fundamental physics parameters and detector parameters that dictate interpolation between elements. Given the quality of the database and the specifications of the detector, only small departures of the measured H value from constancy would be expected, thereby enabling a rather accurate definition of the empirical $k(Z)$ function which refines the interpolation by accounting for any inaccuracies in the database and the detector description.

[31] One change has been made to the PIXE database employed in GUPIX [*Maxwell et al.*, 1995] prior to this work. We include for the first time a chemical bonding dependence of the K-shell fluorescence yields (ω_K) of the four lightest elements (sodium-silicon). This is based upon a PIXE analysis of major element concentrations in a suite of 30 well-characterized minerals [*Campbell et al.*, 1997] assembled by the United States Geological Survey. For the elements magnesium, aluminum and silicon a (7 ± 2) % difference was observed between analyses using silicate minerals and using pure element standards. No such effect was observed for potassium, calcium and iron. This observation suggests that oxide bonding increases the pure element ω_K values for these three elements; a simple statistical calculation [*Larkins*, 1971] of X-ray and Auger decay rates supports this and suggests that sodium will exhibit a similar effect.

6. Determination of H Value

[32] By choosing an H value of 0.0419, we obtain a mean R(Si) value in the four SiO and SiO_2 samples of 1.00. Each of the four contributing R(Si) values has statistical counting error 0.65% (1 sd), but geometric uncertainty is significant (see section 5) given that there are only four pure silicon oxide materials. The corresponding weighted mean value for silicon in 25 GRMs is 1.00 (sd = 0.033). The R value for silicon in the iron formation material IF-G was clearly anomalous at 1.57; this standard was dropped entirely from further consideration. The level of agreement between the two groups is most encouraging. We shall therefore employ the H value of 0.0419 in the full data analysis that follows in sections 7–9.

7. Results for Simple Chemical Materials

[33] Table 3 gives details of the elements and compounds used, their physical form, and the measurement conditions.

Table 3. Measured *R* Values for Chemical Elements and Compounds[a]

Z	Material	Form	Pressure	*R*
11	NaCl	P	0	0.880
11	NaCl	P	10	0.852
11	Na_2CO_3	P	0	0.889
11	Na_2CO_3	P	10	0.912
12	MgO	P	0	0.994
12	MgO	P	10	(0.715)
12	$MgSO_4$	P	0	0.929
12	$MgSO_4$	P	10	0.959
13	Al_2O_3	P	0	(0.875)
13	Al_2O_3	P	10	(0.892)
13	Al_2O_3	S	0	1.00
13	Al	S	0	1.024
14	SiO_2	P	0	0.990
14	SiO_2	P	10	0.963
14	SiO	S	0	1.011
14	SiO	P	0	0.987
15	$Ca_5(PO_4)_3OH$	P	0	0.870
15	$Ca_5(PO_4)_3OH$	P	10	0.859
15	$Ca_3(PO_4)_2$	P	10	0.880
16	$MgSO_4$	P	0	0.923
16	$MgSO_4$	P	10	0.962
17	NaCl	P	0	0.969
17	NaCl	P	10	0.943
19	K_2CO_3	P	10	(0.85)
20	$CaCO_3$	P	0	1.029
20	$CaCO_3$	P	10	1.019
20	$Ca_5(PO_4)_3OH$	P	0	1.004
20	$Ca_5(PO_4)_3OH$	P	10	1.004
20	$Ca_3(PO_4)_2$	P	10	1.063
22	TiO_2	P	0	0.990
24	Cr_2O_3	P	10	1.012
25	MnO	P	10	0.984
26	Fe	S	0	1.007
26	Fe_2O_3	P	0	1.011
26	Fe_2O_3	P	10	1.007
28	Ni	S	0	0.978
28	NiO	P	10	0.995
29	CuO	P	10	0.961
30	ZnO	P	10	1.037
37	$RbNO_3$	P	10	1.075
38	$Sr(NO_3)_2$	P	10	1.062

[a]Physical form is powder (P) or solid (S). The analysis chamber pressure is in mbar units. Parentheses indicate outliers which are discussed in the text.

The majority were in powder form, thereby emulating the GRMs. A few were in solid form, either as metals or as sputtered oxides; these samples had been placed approximately 1 mm closer to the detector than the powders.

[34] The elemental concentrations in all these samples were determined using the system *H* value determined in section 6. As expected, the results for the solid samples were systematically larger than the expected values. From the mean difference we deduced that the solid angle, and hence the *H* value, for these solid materials was larger by a factor 1.073 than for the powders. The solid sample *R* values in Table 3 have been corrected downward by this factor to remove the geometric difference. The statistical uncertainty from the fitting program is typically 1–2%; as discussed above there is a further uncertainty of about 2% arising from sample positioning.

[35] These results show constancy with atomic number except for a few anomalies (in brackets) and in two specific regions of atomic number that are discussed below. The K_2CO_3 datum departs markedly from the trend in that region, and we have no choice but to consider this as due to an undefinable experimental error. There is a similar effect for one of the MgO points. The two points taken with alumina powder fall below the trend in that region; a potential cause is alumina's large capacity for water absorption, and again we feel that it is justified to reject these two data points. The slightly high values for rubidium and strontium might be attributed to the overlap of their X-ray lines with the Compton- and Rayleigh-scattered Lα X-ray lines from the ^{244}Cm source. Four of the calcium results are mutually consistent and in agreement with the overall trend, while that from calcium phosphate is high; we therefore normalized the phosphorus and calcium *R* values in this case such that its calcium value was made equal to the mean of the other four calcium values. The resulting phosphorus value was then in agreement with the phosphorus values from the apatite.

[36] The average values of *R* for each element are plotted against atomic number in Figure 3; the empirical fit is based on the following analysis of these results. The general constancy with atomic number suggests that our database is accurate. But there are two exceptions to this constancy, the first of which is the falloff in *R* below $Z = 13$. One possible explanation of this, mentioned in section 5, is the lack of a perfectly smooth sample surface in these powdered materials. However, we observe a similar falloff with decreasing *Z* for the three elements phosphorus, sulfur and chlorine. In each of these cases the second element of the compound used (calcium, magnesium and sodium respectively) follows the overall $R(Z)$ trend in its own region, which we see as supportive of the phosphorus, sulfur and chlorine data points. This second exception is very suggestive of the existence of a thin silicon layer of incomplete charge collection (ICC layer) on the detector surface [*Campbell and Wang*, 1991] whose absorption of X rays would increase as the photon energy decreases toward the silicon K absorption edge (1.84 keV); the detection efficiency would decrease concomitantly and then increase for the case of the silicon K X rays. The data suggest a layer thickness of about 0.1–0.2 μm.

[37] Such an ICC layer would also explain a large part of the behavior for the very lightest elements, reducing the need for recourse to arguments about surface roughness. We therefore have the option of adding an ICC layer to our computation routine for the detector's efficiency, but our preference is to delay implementation of this detector correction for three reasons. First, a focused study of the detector efficiency and lineshape is required to provide solid support for this idea. Second, chemical bonding may alter the K shell fluorescence yields of phosphorus, sulfur and chlorine. Third, we believe that further experimental and theoretical work is needed to solidify our knowledge of helium ionization cross sections for the lightest elements. Instead, we shall, for the moment, take the empirical approach of absorbing the departures from constancy into the correction function $k(Z)$ that was introduced in equation (4).

8. Preliminary Results for Geochemical Reference Materials

[38] Two issues require examination prior to a full presentation of the results for all elements in the GRMs. The first of these is the possible augmentation of the measured

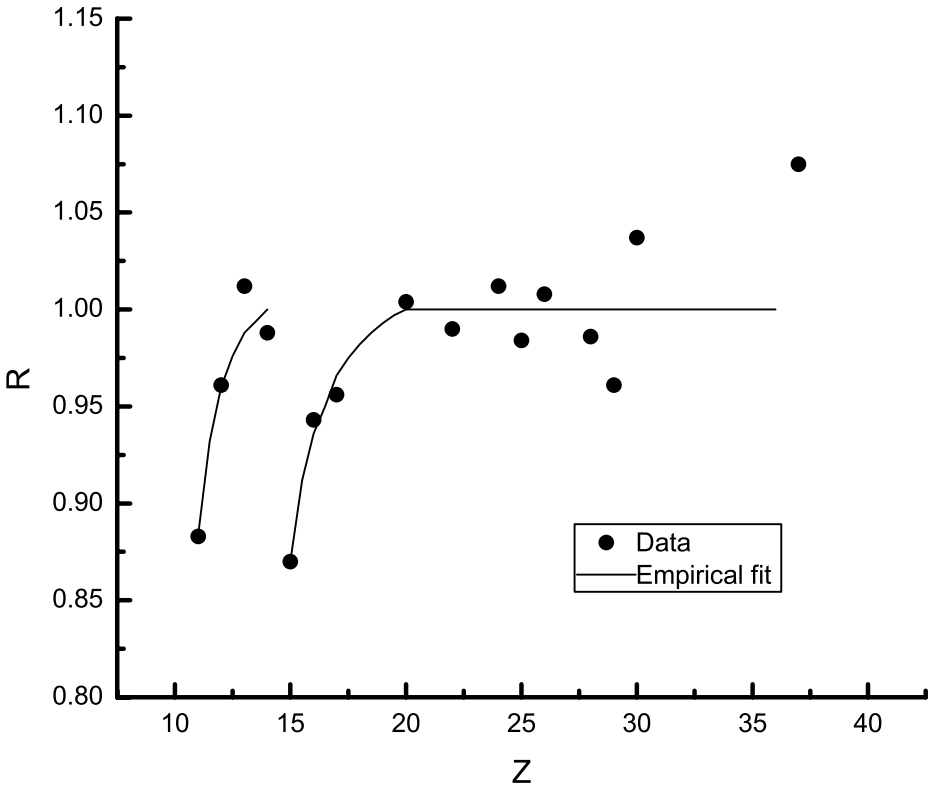

Figure 3. Mean *R* values for pure elements and simple chemical compounds.

X-ray intensities by contributions that do not arise within the sample but are contributed by the materials of the instrument. The second issue became apparent at the end of our first round of analysis of the GRM spectra. Several elements, such as silicon, were well behaved, with excellent agreement of the results across the entire suite. Some other elements, however, departed markedly from such behavior. Preliminary examination of two examples of these behaviors will assist in developing a presentation of the full result set (section 9) that will underpin our attempts to understand departures from uniform behavior.

8.1. Concentration Offsets

[39] Instrumental contributions to X-ray peak intensities arise as follows. Titanium K X rays are excited by PIXE and XRF in the titanium cover foils that protect the ^{244}Cm sources and can then be scattered off the sample and into the detector. Plutonium M X rays from the ^{244}Cm sources are scattered off the sample and into the detector; they overlap in energy with the K X rays of potassium and calcium, and increase the apparent concentration of these elements. Zirconium K X rays are fluoresced in the detector's collimator by the plutonium Lβ and Lγ X rays from the source; some of these are followed by zirconium L X rays from the atomic deexcitation cascade, and there is also excitation of L X rays by sample photons incident on the collimator. The zirconium K X rays from the collimator prevent accurate analysis for this element at the concentrations that are typically encountered in the GRMs. The zirconium L X rays overlap the K X rays of phosphorus. There are very small contributions of copper K, nickel K, and lead L X rays which are fluoresced in structural components of the APXS.

[40] Figure 4 shows the relationship between the GUAPX result for titanium concentration and the suppliers' concentration values for those GRMs in which this element was detectable. The data have been fitted with a linear function. For titanium, the intercept on the vertical axis indicates that there is an instrumental contribution equivalent to a sample concentration of (0.294 ± 0.015) wt % titanium. The other concentration offsets are small: 0.02% for phosphorus, 0.14% for potassium, 0.11% for Ca, 14 ppm wt for nickel, 12 ppm wt for copper and 20 ppm wt for lead.

[41] In this approach to instrumental contributions we have chosen to work in terms of concentration as opposed to peak area, the latter being the approach of *Gellert et al.* [2006]. Peak areas depend upon sample to instrument distance: if the peak area offset is determined at a specific distance, then it must be renormalized to match varying distances during Martian analyses, and that requires some estimate of these distances. This was done [*Gellert et al.*, 2006] via the factor that was required to normalize oxide concentrations to 100% total; this procedure is acceptable if no ''invisible'' light elements are present in the sample, but not otherwise. The disadvantage of our concentration-based approach is that the entire peak area is made subject to the matrix correction, and clearly the instrumental contribution should not be so corrected. However, the effect itself is a small one and so the uncertainty caused by this approximation is not a serious issue. Both approaches share the defect of ignoring the fact that the instrumental contributions are actually sample-dependent, insofar as they are induced by X rays scattered off the sample and the scattered intensity depends upon the constituents of the sample. This is again expected to be a small effect.

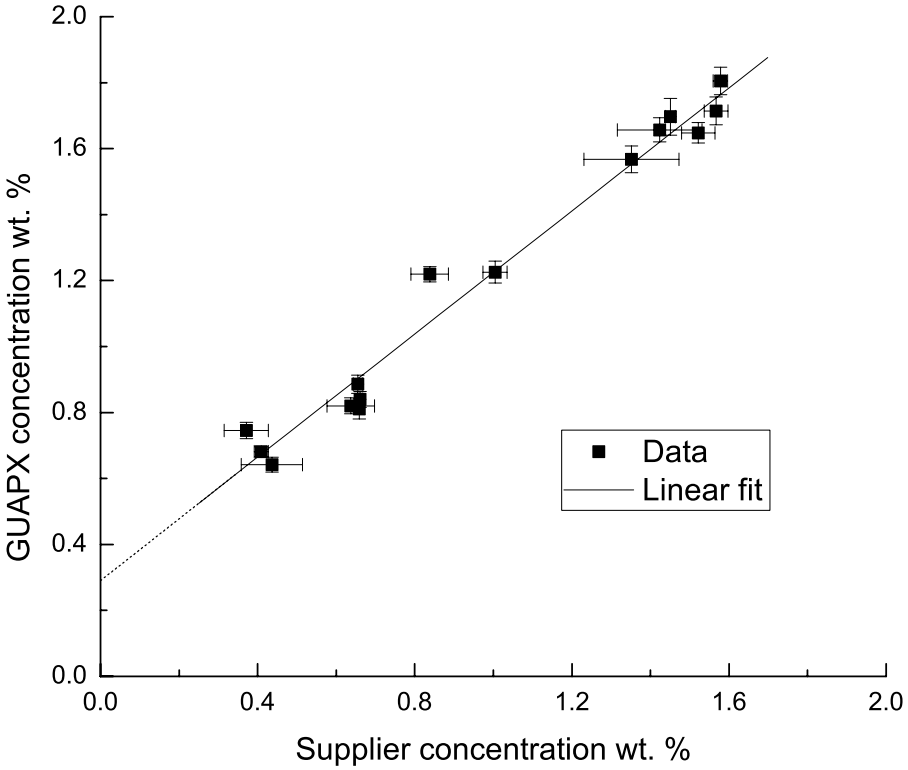

Figure 4. Relationship between fitted and suppliers concentrations for titanium.

8.2. Preliminary Analyses for Silicon and Aluminum

[42] Plots of the *R* values versus the suppliers' concentrations for silicon and aluminum are presented in Figure 5, and provide, respectively, examples of expected and unexpected behavior. The results for silicon cluster around a weighted mean value of 1.000. The average uncertainty (63% confidence level) for any individual determination is about ± 0.006, whereas the overall standard deviation of the set of *R* values for the GRMs is 0.033. A large part of the difference between these two numbers is probably due to the slight variations in sample detector distance that were discussed above.

[43] In contrast, the aluminum results are widely scattered. Spectrum fitting issues might be expected to cause divergence from 1.0 as very low concentrations are approached, but the three results at lowest aluminum content do not sustain that argument. A more convincing argument can be marshaled on the basis of Figure 6, where we plot the *R*(Al) values versus the SiO_2 content for six distinct subgroups of the GRM suite, namely, four igneous rock types, pure minerals, and the synthetic glass. For the seven minerals and the glass, the weighted mean *R* value is 0.990, in good agreement with the mean chemical standards value (1.01) of Figure 3. In contrast with the almost constant behavior of the minerals, the basalts, andesites and rhyolites exhibit a decreasing linear dependence upon SiO_2 concentration. These two dramatically contrasting behaviors suggest that the scatter of the aluminum results in Figures 5 and 6 is not an instrumental or spectrum fitting issue. The dependence on silica content led to the tentative suggestion (P. L. King, private communication, 2008) that different APXS calibrations might be appropriate for different rock types. For the igneous rocks in particular, P. L. King suggested using a total alkali-silicate (TAS) diagram to define the igneous subgroups as shown in Figure 7. The two very similar basalt materials BE-N and BR lie just outside the basalt region in the diagram, but we treat them here as belonging to the region. Similarly, we include the granite GH in the rhyolite-dacite class. Despite its nomenclature, the U.S.G.S. Columbia River Basalt BCR-1 falls within the andesite class on the diagram. These three igneous subgroup definitions are used in the presentation of the full set of results in section 9.

[44] The igneous rock AN-G (anorthosite) does not fit within this scheme and is therefore treated on its own merits. The AN-G data point on Figure 6 is in better agreement with the pure mineral behavior than the igneous rock behavior, a result that will be explored in section 10. The remaining GRMs are divided into three further subgroups, namely, sediments, an artificial glass, and a subgroup of two others.

9. Results and Commentary for the Entire Suite of GRMs

[45] In the following plots of *R* values versus suppliers' concentrations for the various elements, different symbols will be used to denote the subgroups of GRMs defined in section 8. In the cases where concentration offsets are present, these have been corrected for within GUAPX. Each elemental plot displays data for those GRMs in which that element's concentration exceeds the detection limit sufficiently that statistical uncertainty is tolerable; this enables us to focus on issues of peak fitting, physics database and geochemical effects.

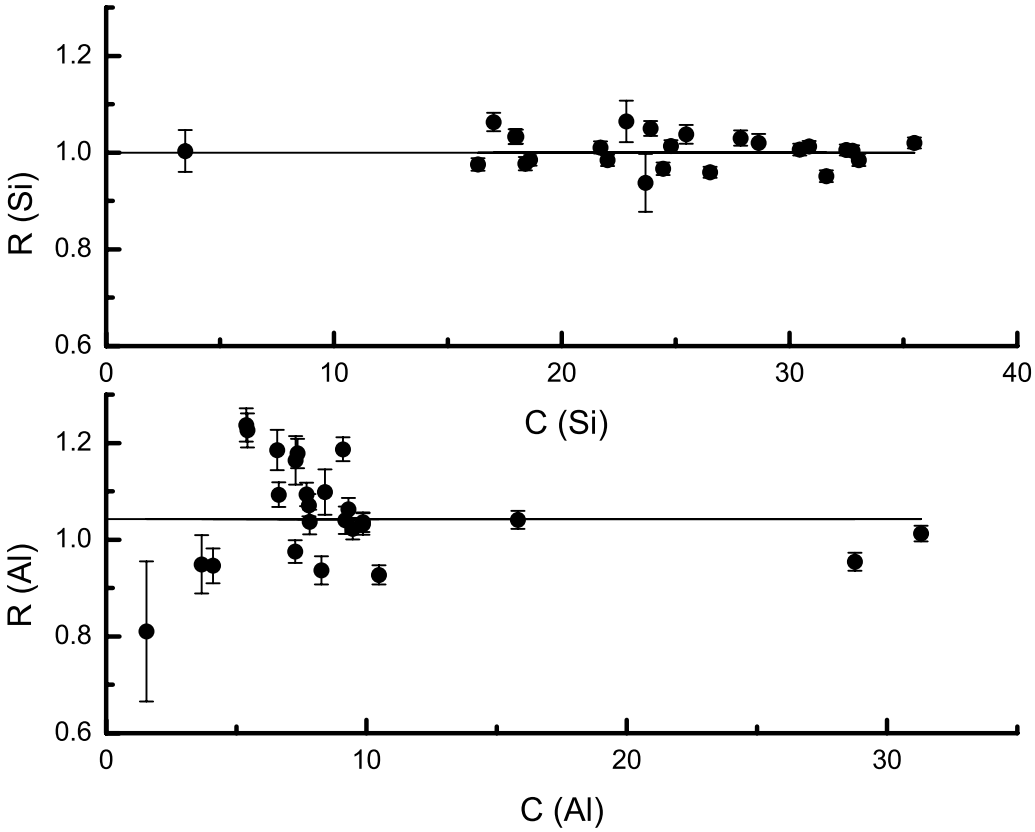

Figure 5. Relationships of *R* values and concentrations *C* for silicon and aluminum.

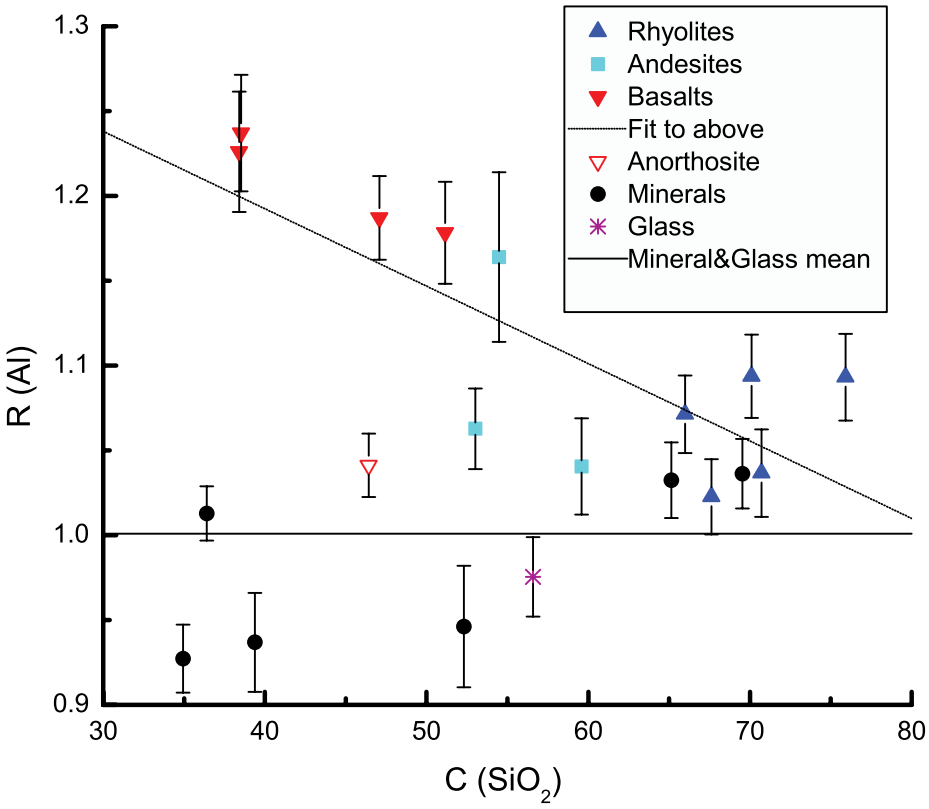

Figure 6. *R* (Al) as a function of SiO_2 concentration in some of the geochemical reference materials (GRMs).

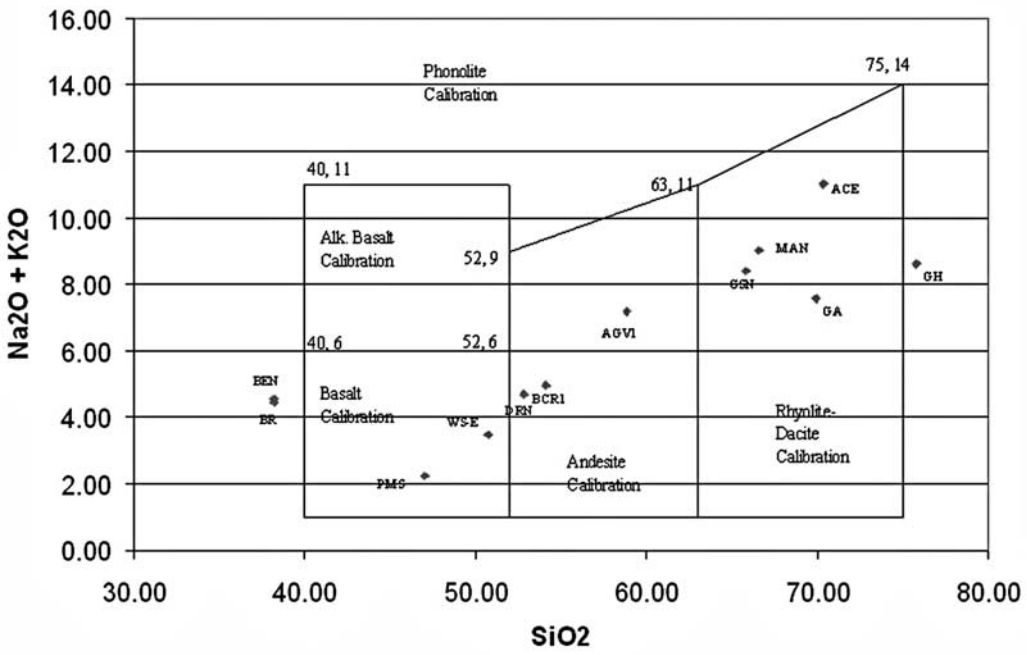

Figure 7. Total alkali versus silicate content diagram for igneous GRMs used in this work and showing regions of potentially different calibration.

9.1. Sodium, Magnesium, Aluminum, and Silicon

[46] In Figure 8 we show the results for the four elements of lowest atomic number, all being major elements and all being analyzed essentially 100% by PIXE. The small value of analyzed depth, a few microns, should be borne in mind. As already noted, the weighted mean R value for silicon is 1.000 (sd 0.033), with much of the standard deviation being attributable to geometric placement and fitting uncertainties.

[47] Sodium and aluminum exhibit similar behavior to one another, a behavior that is dramatically in contrast to that of silicon. The weighted mean value R_{wm}(Na) is 0.990 (sd 0.12), considerably exceeding the mean value of 0.883 for the simple chemical materials. For aluminum the R_{wm} value of 1.043 (sd 0.10) exceeds only slightly the value from Table 3 for the chemical compounds. There are no obvious outliers in either case, but there is a very large scatter of the data. The subgrouping of the igneous rocks enables us to see a pattern within the scatter. For aluminum the mean basalt result lies about 20% higher than the value of $\sim$1.0 expected from the simple chemical compounds, but the mineral group is in good agreement with that expectation; the andesite and rhyolite results fall between the two extremes. The pattern for sodium is qualitatively similar: here the mean basalt result is 30% higher than the chemical compound result and the mean andesite result 13% higher; the mineral result of 0.96 is the closest to the value of 0.88 found in the chemical compounds but it does not reach agreement.

[48] The anorthosite result is close to that of the basalts for sodium, but for aluminum it follows the rhyolite results. Apparently, the rock type which hosts sodium and aluminum, influences their R values, a finding which will be explored in detail in section 10.

[49] For magnesium, the weighted mean R value is 0.90 (sd 0.12), which agrees within rather large uncertainties with the result of 0.96 (see Table 3) from the chemical compounds. For concentrations above 2% the weighted mean has the same value but half the uncertainty. The increasing scatter and larger error bars toward the left side of the plot illustrate the challenge to the fitting program in extracting an accurate intensity for the magnesium peak, which is superposed upon the combined low-energy tail of the intense aluminum and silicon peaks. There is no strong evidence in this case for a dependence of R value upon rock type.

9.2. Potassium, Calcium, Titanium, and Iron

[50] For the four major elements discussed here, the PIXE fraction decreases rapidly, reaching about 10% at iron. The analyzed depth undergoes a concomitant large increase. The results are shown in Figure 9.

[51] For potassium, after compensation within GUAPX for the concentration offset, the weighted mean R value is 1.026 (sd 0.047). The weighted mean value for R(Ca) in the GRMs is 1.043 (sd 0.038). The two rhyolite points at the left of the calcium plot (GA, GS-N) are the two GRMs with the highest K/Ca concentration ratio among those materials in which both these elements are detectable. A small error in our database value for the potassium Kβ/Kα X-ray intensity ratio would cause error in the extraction of the calcium Kα intensity from the overlapping calcium Kα and potassium Kβ peaks; this may explain the tendency of these two points to exceed the mean. The potassium content of Martian rocks is much lower than on Earth, and so the database issue that causes the calcium data points for GA and GS-N to lie a little high is not expected to be replicated in analysis of Martian samples.

[52] As indicated above, titanium has a concentration offset of 0.29 wt %; making allowance for this, the R_{wm} value is 0.93 (sd 0.09). For iron we have R_{wm} = 0.984 (sd 0.035). There are very large uncertainties in the points for the four

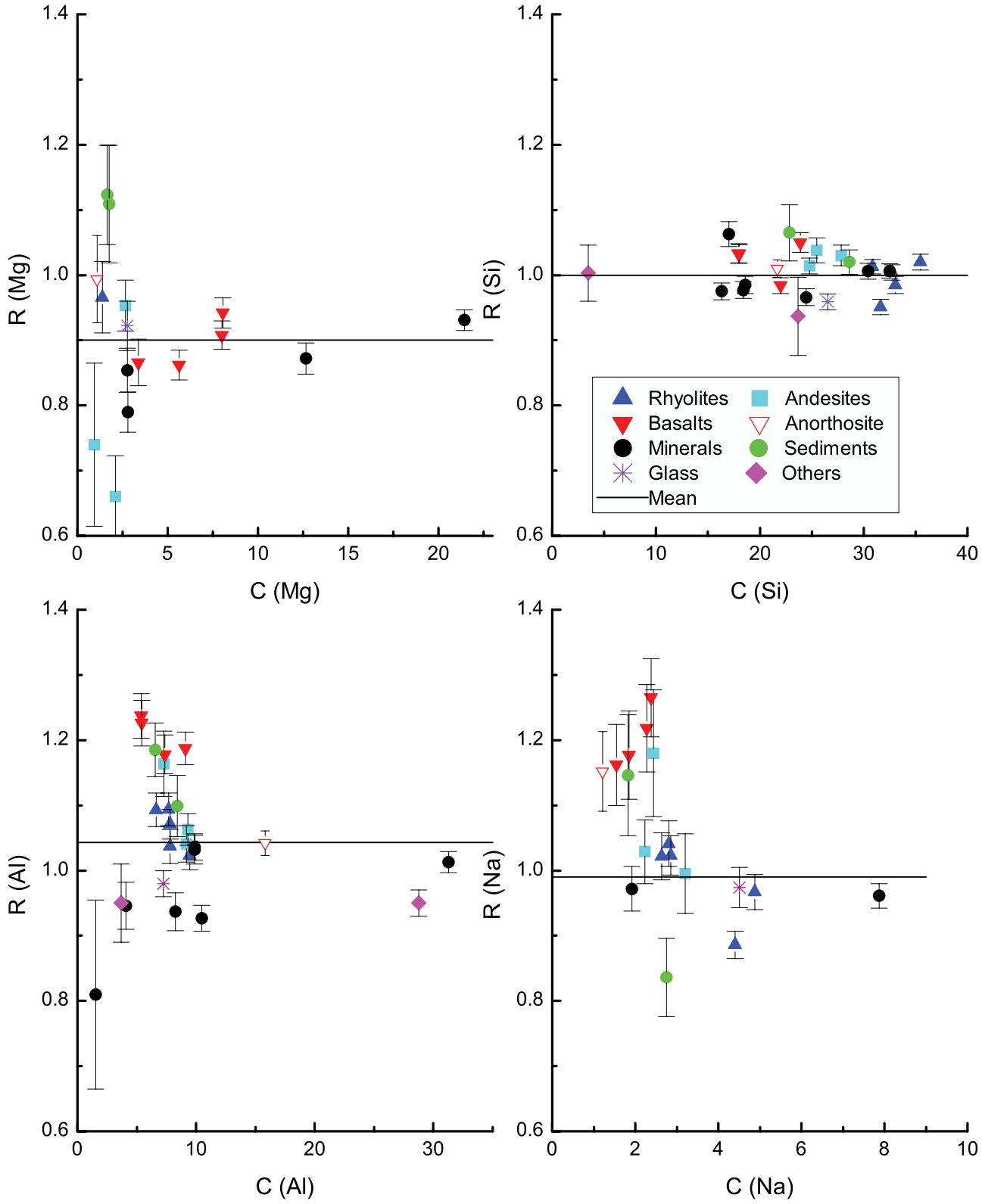

Figure 8. *R* values in the GRMs plotted against concentration *C* in wt % for the elements Na, Mg, Al, and Si. The horizontal line is the error-weighted mean.

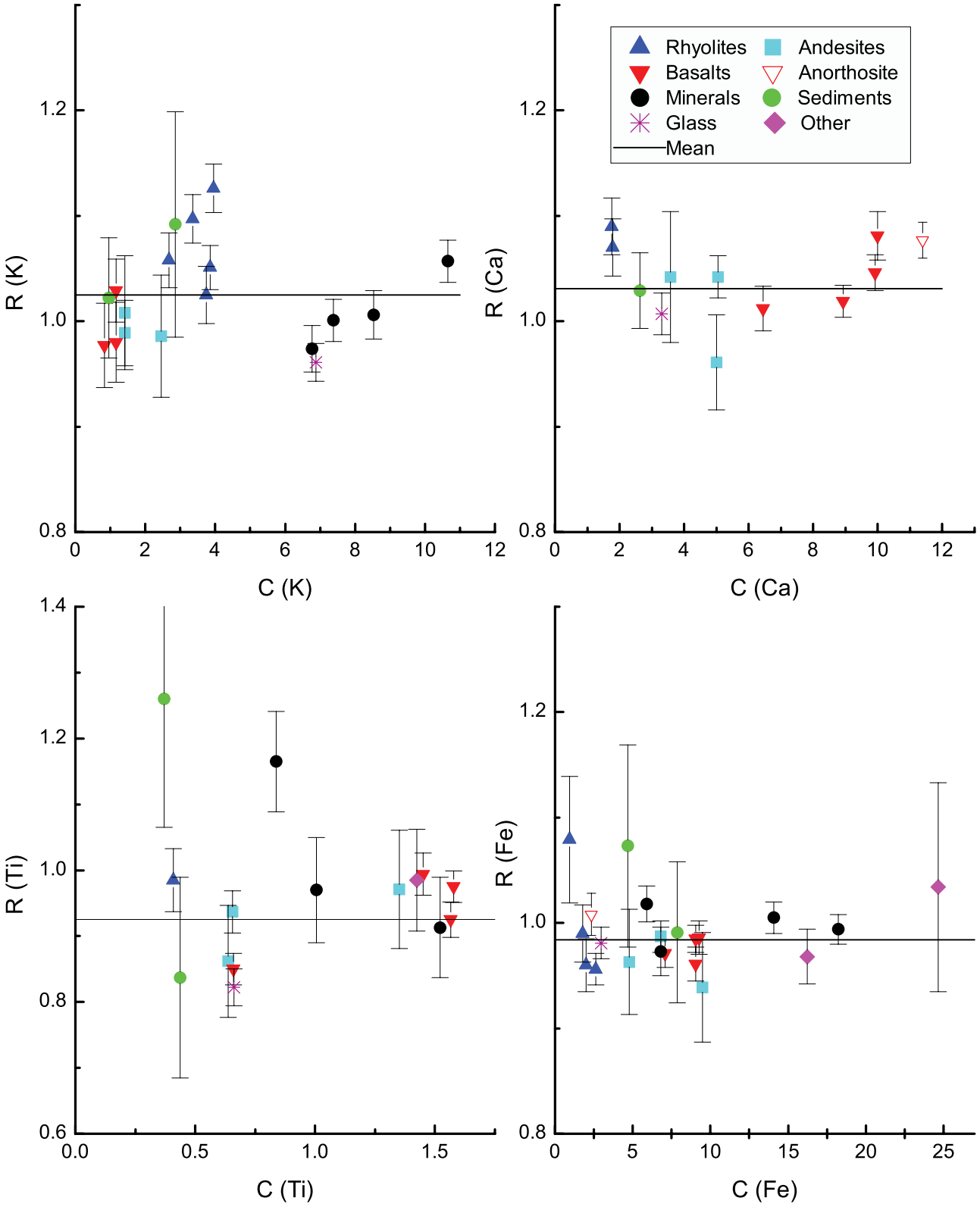

Figure 9. *R* values in the GRMs plotted against concentration *C* in wt % for the elements K, Ca, Ti, and Fe. The horizontal line is the error-weighted mean.

low iron concentration materials AL-I, DT-N, FK-N and MA-N, and so we have excluded these from the plot; their exclusion does not alter the value of R_{wm}(Fe).

9.3. Phosphorus, Sulfur, Chlorine, and Bromine

[53] Each of these four elements occurs in only a small subset of the GRMs. Phosphorus is a minor element while chlorine, bromine and sulfur are trace elements in terrestrial GRMs. As a consequence, the uncertainties in R values are large. Calibration for each of these elements is important, given the evidence that they provide for aqueous processes in the geological past [*Brückner et al.*, 2008; *Ming et al.*, 2008]. The results are in Figure 10.

[54] The presence of the zirconium L X-ray peak under the phosphorus peak gives rise to an offset in the plot of GUAPX concentrations versus the suppliers' concentrations. As indicated above its value is (0.023 ± 0.01) wt %. As a check, we fitted the spectra of the chemical compounds, including phosphorus in the list of elements possibly present; the average apparent concentration derived from the areas of the fitted phosphorus K peaks (actually zirconium L) was (0.015 ± 0.005) %. The GRM spectra were then processed with a concentration offset 0.02% included. The overall weighted mean result for the rock GRMs is 1.30 (sd 0.13). The only visible trend is that the two mineral data points fall significantly below those of the rocks; these two have a mean R value of 0.87, which agrees well with the trend of Figure 3. This difference between mineral and rock results for phosphorus suggests that in the rocks, the phosphorus is present in the rocks as a distinct mineral phase, possibly apatite, so that the assumption of homogeneity fails.

[55] The sulfur R values have large uncertainties and exhibit a large degree of scatter, because the concentrations involved are at the trace level and the suppliers' concentration values have large uncertainty estimates. With the exclusion of the highly discrepant UB-N result ($R = 2.7$) from the plot, the weighted mean R value is 0.97 (sd 0.28). The chlorine case is also one of high scatter, with all but one of the GRMs concerned having concentrations less than 0.1%; the overall R value is 1.19 (sd 0.23). The exception for chlorine is the sediment MAG-1 (3 wt% concentration), whose R value of 0.87 agrees well with the value established for the chemical compounds. Bromine is included in this section because of the obvious linkage between chloride and bromide salts. However, bromine is detectable in only a single GRM, again MAG-1, with a low (250 ppm wt) concentration; this single R value is 1.02 but has an uncertainty of 28% (sd) arising mainly from the large uncertainty quoted by the USGS.

9.4. Chromium, Manganese, Nickel, and Zinc

[56] These four elements are minor and trace elements, occurring at concentrations less than 0.3%. Figure 11 shows the chromium results for the small number of materials where the concentration exceeds 0.02%. At lower concentrations in the vicinity of the detection limit, the R values fluctuate owing to large statistical errors. The mean value of R is 1.11 (sd 0.10), in agreement with Figure 3.

[57] The manganese peak has low intensity compared to the neighboring iron peak and is superimposed upon the low-energy tail of the latter. The parameters of this tail were determined from fits to pure iron spectra, and for the GRM fits they are fixed in proportion to those of the main Gaussian peak. The fitting uncertainty in the iron Gaussian height is ∼1% and so this is also the fractional uncertainty in the tail height. However, the manganese peak height is typically 100 times smaller than the iron peak height. The iron tail uncertainty therefore makes a large contribution to the uncertainty in the manganese peak height, which is why the uncertainties in individual manganese R values are large: on average ± 14%. The weighted mean R value is 1.035 (sd 0.07).

[58] For zinc, the error bars are large, ranging from 5 to 25%, in this case reflecting the small concentrations; the BX-N data point at $R = 0.68$ appeared anomalous and was excluded from the plot. The zinc weighted mean R value is 1.00 (sd 0.07). In the nickel case, a concentration offset of 14 ppm wt was deduced from the observed relationship between measured and suppliers' concentrations. The plot is restricted to points having individual uncertainties below 40%. The weighted mean R value is 1.13 (sd 0.11); if we restrict discussion to the two points having the highest concentrations, the same value emerges.

9.5. Trace Elements

[59] This final group comprises nine trace elements whose concentrations are typically around or under 0.1%. The results for copper, gallium, strontium and lead are in Figure 12. In the case of copper, where a 12 ppm wt offset was subtracted, the reference materials having the lowest concentrations show a wide but symmetric scatter that reflects the statistical uncertainty of individual values. The overall mean R value is 1.15 (sd 0.13). Two data points at the high end of the concentration range offer much smaller uncertainties, and their mean is 1.055. There are only seven useful data points for gallium, of which six have individual uncertainties 7–28% while the BX-N datum has ∼45% uncertainty. However, the outcome is encouraging, with an R_{wm} value of 1.04 (sd 0.18). For strontium we limited ourselves to cases having concentrations above 0.02%. Here we see a clear trend of rising R value with increasing concentration; we attribute the low R values at low concentrations to error in separating the strontium K X-ray peak from the overlapping, and more intense, Rayleigh scatter peak of the 14.26 keV Lα photons from the source. If the averaging is limited to cases with concentration above 0.05% in order to decrease the scatter, the weighted mean R value is 0.97 (sd 0.07).

[60] Lead is detected via its L X rays, which span a wide energy range. Differing absorption means that the L X-ray intensity distribution will be different between the spectrum contribution from sample lead and from that fluoresced within materials of the APXS. For this reason the fitting code treats lead as separate "subelements" Pb Ll, Pb Lα, Pb Lβ, and Pb Lγ, whose spectral contributions are not correlated through literature relative intensities; the lead concentration is derived from the area of the lead Lα peak, which is in fact the pure L3M4,5 X-ray line. The BX-N point had $R = 2.0 \pm 0.9$ and was excluded, in yet another example of anomalous results from this material. The mean value of the plotted data points is 1.15 (sd 0.26). It needs to be noted that the element arsenic, whose Kα X-ray line overlaps the dominant lead Lα line, was not included in the list of elements to be fitted, apart from the single exception (see below) where arsenic was known to be present in detectable amounts. Thus the analysis for lead is somewhat

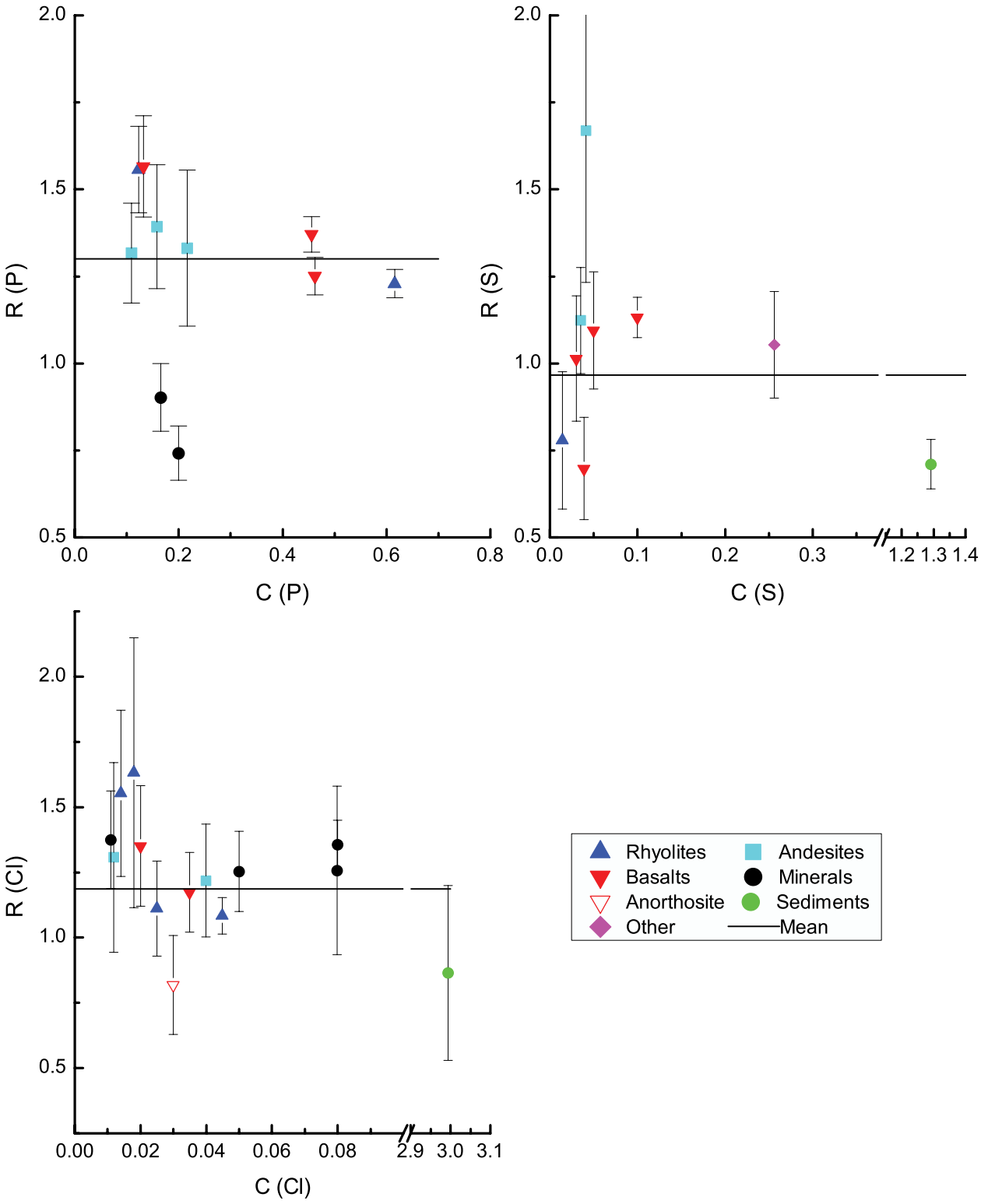

Figure 10. *R* values in the GRMs plotted against concentration *C* in wt % for the elements P, S, and Cl. The horizontal line is the error-weighted mean; in the phosphorus case it is computed for the rock GRMs only.

idealized, but it serves its present purpose of testing the lead database and fitting procedure.

[61] The element rubidium is a difficult case. It is detected via its Kα X-ray line, which overlaps with the broad, asymmetric Compton scatter feature from the plutonium Lα photons. Nevertheless, for materials with concentration exceeding 0.2%, the weighted mean *R* value is 1.08 (sd 0.13). Yttrium is an even more difficult challenge. Its Kα X-ray line overlaps the Kβ line of rubidium, whose correlated Kα line suffers, as already mentioned, from

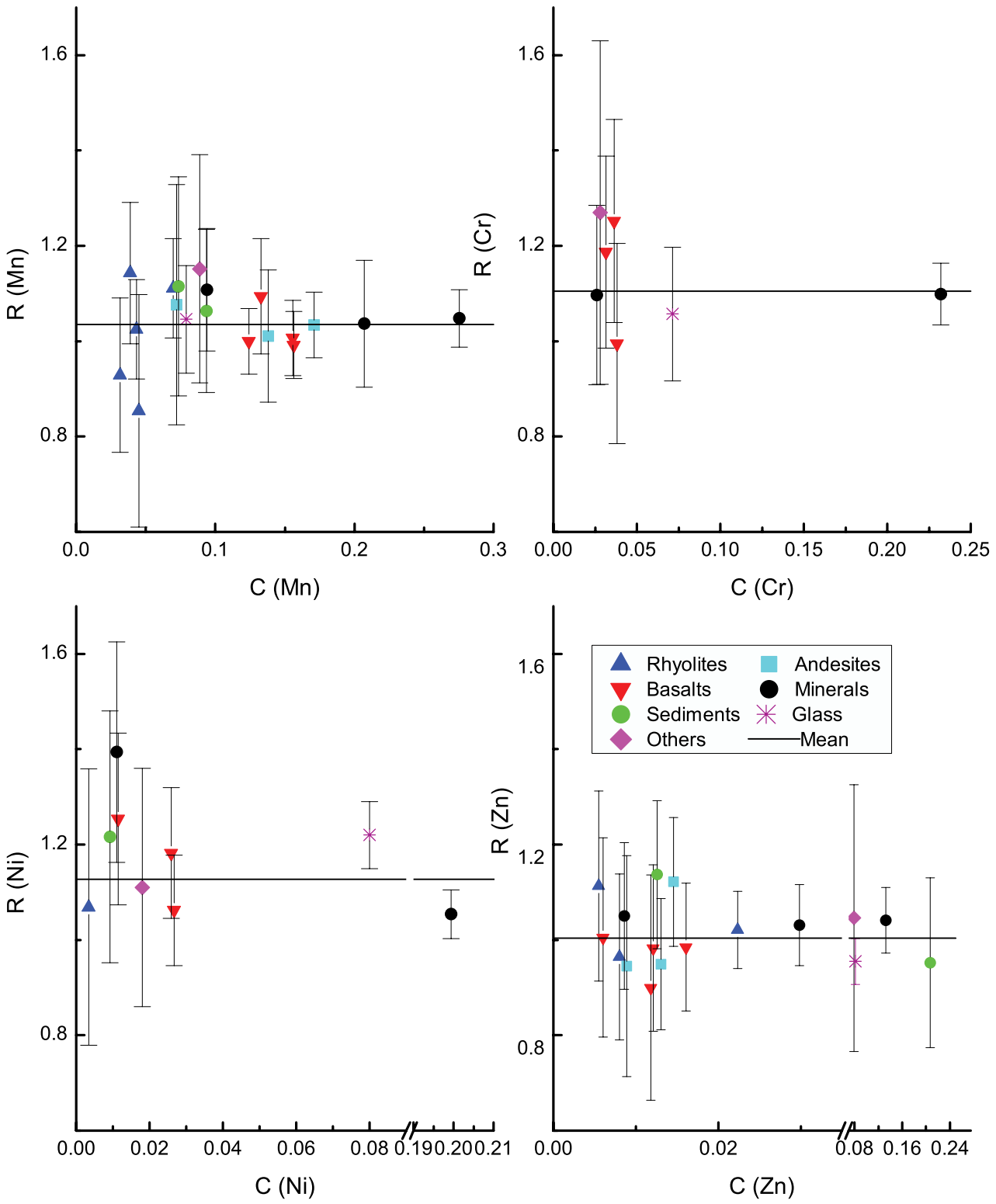

Figure 11. *R* values in the GRMs plotted against concentration *C* in wt % for the elements Cr, Mn, Ni, and Zn. The horizontal line is the error-weighted mean.

overlap with the Compton feature. If we confine ourselves to the four cases having highest yttrium concentration (>0.08%), we find an average *R* value of 1.08 (sd 0.0.04). Arsenic was detected in only one material (GXR-1), with an *R* value of 0.94 ± 0.15.

[62] Two further trace elements are detected by their L X rays. Tungsten is definitely determined in just five materials (AN-G, DR-N, DT-N, FK-N, GS-N) and the result is R_{wm} = 1.02 (sd 0.15). Inclusion of tungsten in the list of elements to be fitted was important; its neglect would have caused

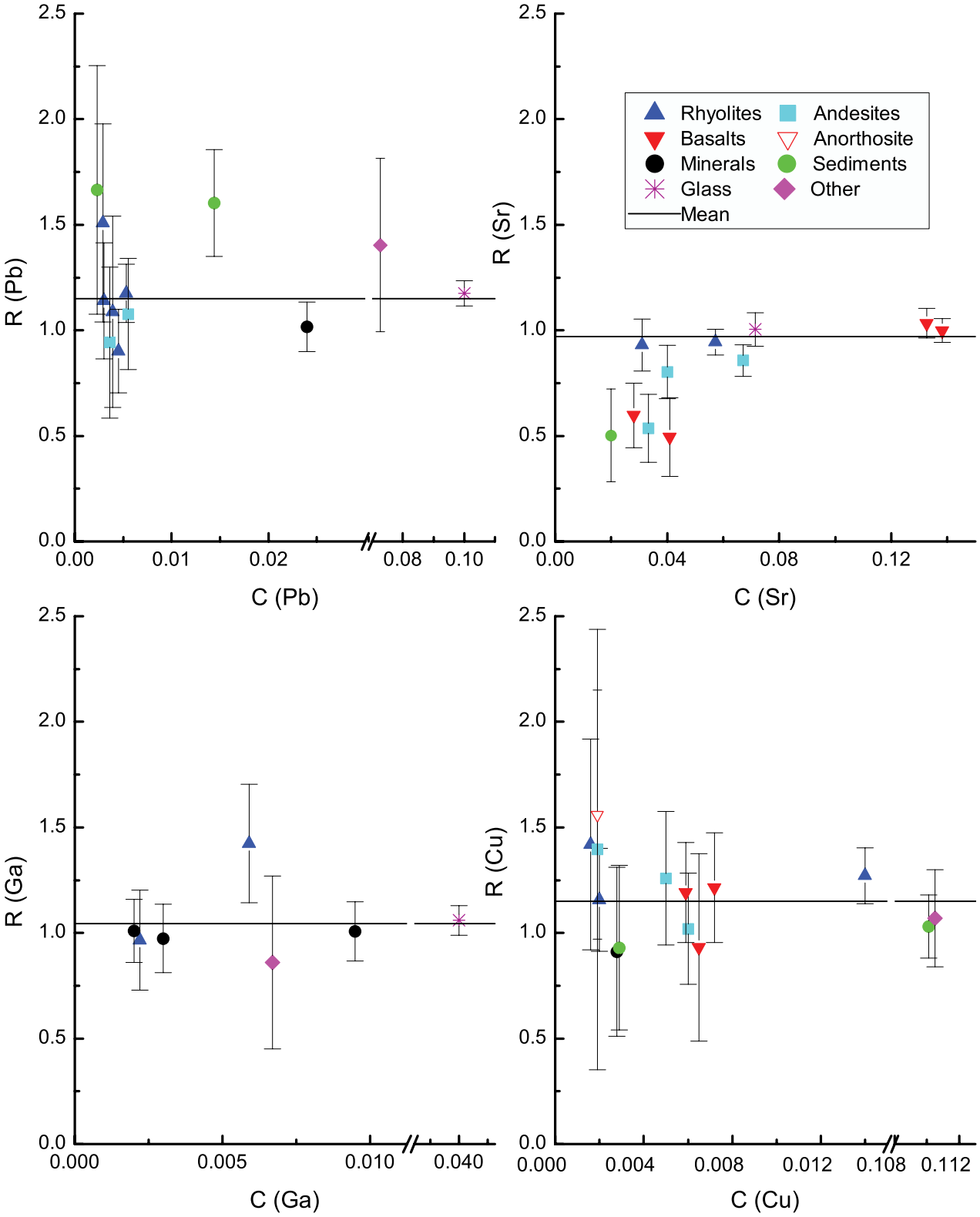

Figure 12. *R* values in the GRMs plotted against concentration *C* in wt % for the elements Cu, Ga, Sr, and Pb. The horizontal line is the error-weighted mean; in the Sr case it is calculated for those elements having $C > 0.05\%$.

significant errors in some of the zinc results. Bismuth is detected in the two cases VS-N and GXR-1, and the official value for the first of these is only provisional, with no attached uncertainty; the average R value for the pair is 1.15. Inclusion of bismuth in the elements to be fitted was important: its neglect causes significant error in the result for lead, whose L X rays overlap the K X rays of bromine.

10. Discussion of the GRM Results

10.1. General Comments

[63] Our R values for the majority of elements in the GRMs that were utilized in the MER APXS calibration report [*Gellert et al.*, 2006] are well behaved. With some exceptions that we shall explore in detail, the scatter in each of the elemental plots (Figures 8–12) can be attributed to counting statistics, spectrum fitting issues and small geometric variations. For the major elements silicon, potassium, calcium and iron, the agreement between our mean measured concentrations and those given by the suppliers is within 5%, which suggests that the PIXE and XRF databases are accurate to that level. For the major element magnesium, a superficial consideration suggests a 10% discrepancy, but most of this can be attributed to our neglect of an incomplete charge collection layer in the X-ray detector. The inclusion of such a layer or the application of a simple multiplicative correction based on the R values of simple chemical compounds moves the accuracy for magnesium close to the 5% value achieved for silicon, potassium, calcium and iron. For titanium there is a systematic 7% discrepancy: the titanium K X-ray peak overlaps the asymmetric escape peak of the iron Kα peak, which suggests that attention needs to be paid to the accuracy of the escape peak intensity ratio [*Papp and Campbell*, 2001].

[64] For two light major elements, sodium and aluminum, there are discrepancies that appear to reflect igneous rock type and which reach 20% in the case of basalts; these may arise from mineral phase heterogeneity, as discussed in detail below.

[65] In the atomic number region $24 \leq Z \leq 35$, where XRF is the predominant excitation mechanism, every element except iron is a minor or trace element, and the statistical uncertainty is much greater than in the case of the major elements; within these uncertainties there is no indication that the R_{wm} values depart systematically from 1.0. It is for the lightest elements, excited entirely by PIXE, that trends emerge which require more extensive consideration if they are to be understood.

10.2. Mineral Phase Effects for Aluminum and Sodium in GRMs

[66] Sodium and aluminum exhibit essentially the same effect, namely, a dependence of R value upon rock type, with the values decreasing as we move through the igneous rock sequence basalts to andesites to rhyolites to minerals; the lowest R values, namely, those for minerals, agree quite well with the trend established in Figure 3 for pure elements and simple chemical compounds. (We believe that the latter trend is determined in the main by detector properties, although the role of particle size effects for the lightest elements remains to be clarified.) The range of R values is largest for sodium, and in this case spectrum fitting issues cannot be excluded, because the sodium peak is usually of low intensity and also because the electronic cutoff leaves us lacking clear definition of the continuous spectrum background at lower energies. One might suggest that as the neighboring magnesium peak grows in relative intensity, any systematic fitting error in R(Na) might increase, and indeed R(Na) does correlate with magnesium concentration. However, increasing magnesium content in igneous rocks correlates with the progression from felsic to mafic rock types, and so the correlation of R(Na) with C(Mg) may alternatively arise from a dependence of the PIXE analysis upon the specific rock type.

[67] The case of aluminum offers a resolution between these two alternative explanations. Aluminum concentrations in the GRMs are higher than those of sodium, and the theoretical X-ray yield per unit concentration is also higher. The aluminum peaks are therefore more clearly defined than those of sodium, and spectrum fitting errors are much less of an issue. Figure 6 showed that there is a decreasing linear relationship between R(Al) and the silica concentration for the three igneous rock types basalt, andesite and rhyolite, in contrast with an essentially flat behavior for the minerals over the same wide range of C(SiO_2).

[68] We suggest then that the particulars of the mineral assemblage within the rock are responsible for the unique behavior of R(Na) and R(Al) in the igneous rocks. For andesites, and more so for basalts, the sodium and aluminum occur mainly within minority feldspar or plagioclase phases, with the majority phase being pyroxene or olivine. Our assumption of a homogeneous matrix then results in the matrix terms of equation (4) being calculated by GUAPX approximately as if these two elements were located within the majority phase. This explanation of the sodium and aluminum results is supported by fundamental physics calculations of ion-induced X-ray yields from different matrices using the GUPIX subroutines. We first computed the quantity $Y_{1,PIXE}$ (Na) for pure sodium feldspar; this quantity, defined in the discussion of equations (1–4), describes the matrix effects for sodium in feldspar in the PIXE process. We then performed the same computation for orthopyroxene, but with 2 wt % of sodium incorporated; $Y_{1,PIXE}$ (Na) was 34% less in the pyroxene. We now consider a highly simplified model basalt containing only two phases, a minority sodium feldspar phase and a majority pyroxene phase, with sodium and aluminum present only in the former. In practice, GUAPX treats this basalt matrix as if it were a single phase. The matrix calculation that is performed for sodium is thus much more strongly influenced by the element concentrations of pyroxene than those of feldspar. This will result in a $Y_{1,PIXE}$ (Na) value that is too small and hence a sodium concentration value that is too large. We repeated this exercise for aluminum, adding 8% of aluminum to the orthopyroxene. The $Y_{1,PIXE}$ (Al) value decreased by 30%, which would again suggest a significant overestimate of the aluminum concentration. These results are in accord with the observed behavior and thus offer strong semiquantitative support for our hypothesis.

[69] Returning to Figure 6, we see that the case of AN-G (anorthosite) is a clear exception to the R(Al) − C(SiO_2) correlation that was established there for the other igneous rocks. In contrast, the analogous plot for sodium, shown now as Figure 13, shows that R(Na) follows the overall igneous GRM trend. Anorthosite is dominated by the

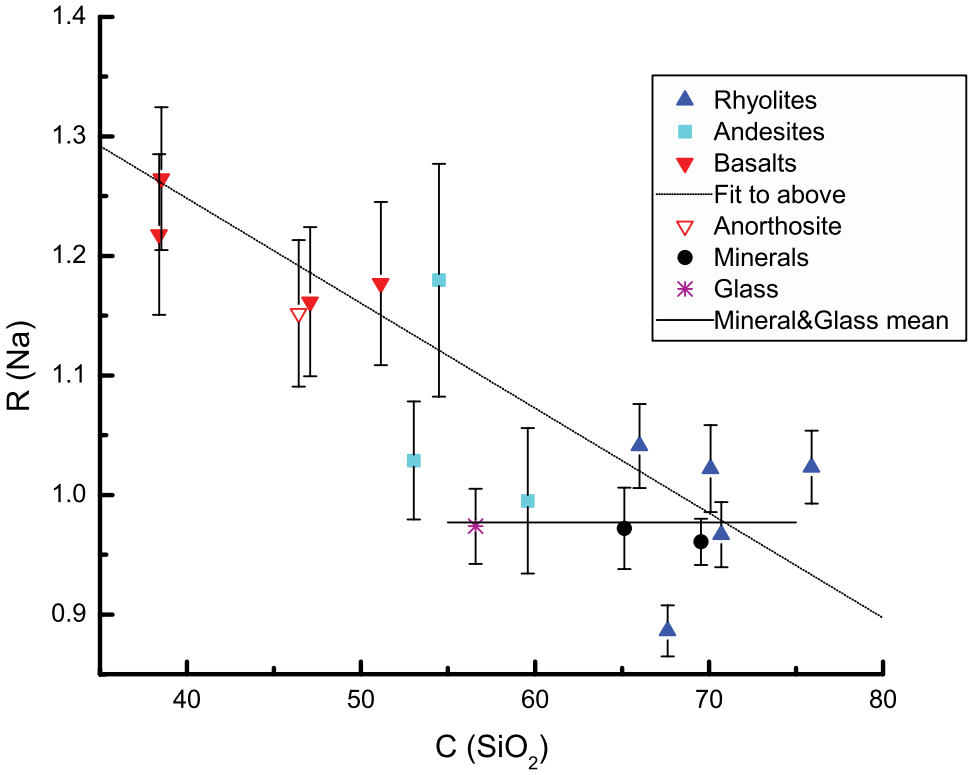

Figure 13. *R* (Na) as a function of SiO_2 concentration in some of the GRMs.

calcium-rich end-member of plagioclase feldspar, and so the sodium resides mainly in the small mafic component. Aluminum, in contrast, resides mainly in the majority, feldspar phase. So, in this case, the matrix terms are computed accurately for aluminum, but not for sodium. The magnesium resides in the majority mafic phase and so it is handled correctly; this is reflected in the proximity of its *R* value to unity.

10.3. Other Mineral Phase Issues

[70] Another example of these matrix effects is seen in phosphorus. The *R* value is well behaved in the two pure mineral GRMs, with a mean value of 0.80, which is consistent with the trend of Figure 3. In contrast, *R*(P) is around 60% higher in various igneous rocks, where it presumably is found in a phosphate phase that is distinct from the main rock matrix.

[71] A similar situation may exist in the case of chlorine, although the large statistical uncertainties here demand caution. While the trend of Figure 3 suggests that *R*(Cl) should lie well below 1.0, the weighted mean value over all the GRMs is 1.19. This might suggest that chlorine is present in a separate salt phase. However, the very large uncertainty of 0.31 (sd) in the *R* value suggests caution in drawing any conclusion.

10.4. Iron

[72] The two elements for which we have the most precise values for R_{wm} are silicon and iron. In neither of these cases do we observe strong mineral-dependent trends such as those observed for sodium and aluminum, and so we feel justified in considering the suite of GRMs as a single population. This permits us to define the uncertainty as the standard error of the weighted mean for the cases of iron and silicon. Having adjusted the system *H* value to ensure that $R_{wm} = 1.000 \pm 0.006$ for silicon, we then find that $R_{wm} = 0.985 \pm 0.008$ for iron. There is thus modest evidence of a 1.5% difference between the observed and expected results for iron. Such an excellent outcome suggests that the physics database of GUAPX, especially the ionization cross-section component, is very accurate, more so than we might have expected.

[73] In contrast however, the chemical compounds show no divergence between silicon and iron results; the mean *R* value over the atomic number range $20 \leq Z \leq 30$ is 0.998, which agrees with the silicon value of 1.00. This slight difference between the two suites may suggest that the slightly lower GRM R_{wm} value for iron arises in some manner from its location within a rock matrix. A modest degree of support for this suggestion is found in the slightly higher iron $R_{wm} = 1.000$ (sd 0.016) obtained for the pure mineral GRMs. No other elements in the GRMs offer the precision in their R_{wm} values to test this idea further.

11. Conclusions

[74] This study is part of an attempt to develop a physics-based calibration procedure which will eventually be applied to the existing Mars Exploration Rover APXS data and which we hope to apply to the Mars Science Laboratory APXS data. It has demonstrated generally good agreement between a calibration based upon pure elements and chemical compounds and one based upon geochemical reference materials.

[75] The differences between these two approaches are largest for the lightest elements studied, and it is in these cases that the specific rock type appears to exert significant

Table 4. Detailed Analysis of *R* Values for Sodium, Magnesium, and Aluminum

	Quantity	Na	Mg	Al
All GRMs	R_{wm}	0.990	0.900	1.043
	$R_m \pm 2sd$	1.06 ± 0.24	0.91 ± 0.24	1.05 ± 0.20
	Range of *R*	1.05 ± 0.21	0.88 ± 0.22	1.08 ± 0.16
GRM subgroups				
Basalts	$R_{wm} \pm$ EEM	1.21 ± 0.06	0.90 ± 0.03	1.20 ± 0.03
Andesites		1.04 ± 0.07	0.86 ± 0.06	1.07 ± 0.03
Rhyolites		0.965 ± 0.025	0.97 ± 0.11	1.06 ± 0.02
Minerals		0.96 ± 0.03	0.89 ± 0.02	0.99 ± 0.02[a]
Pure elements and simple compounds	Range of *R*	0.88 ± 0.03	0.96 ± 0.03	1.01 ± 0.01

[a]Anomalous UB-N *R* value excluded.

influence upon the results. Our explanation for these effects is that certain igneous rocks violate the assumption of homogeneous element distribution within the sample that is basic to our fundamental parameters approach. The explanation is supported in semiquantitative fashion by computations of ion-induced X-ray yields in various mineral phases. This is not a surprising outcome in view of the longstanding recognition of heterogeneity effects within the rock analysis community, which has adopted fusion methods of sample preparation specifically to eliminate these issues. Such an approach is not feasible on a robotic Martian mission and would also result in a loss of the very important detection capabilities for volatile constituents. However, fusion does offer us the possibility of testing our explanation in the laboratory.

[76] Our next objective is to translate the results of the present work into a function $k(Z)$ that applies the necessary correction to the *H* value for each element; this function would then be used directly in GUAPX iterative matrix element solutions for Martian samples. In the preceding data analysis the focus has been on the weighted mean *R* value because this takes a statistically proper account of uncertainties. The simplest approach would obviously be to define $k(Z) = 1/R_{wm}(Z)$ separately for those elements where we have found a statistically valid departure of $R_{wm}(Z)$ from unity. But this approach may be too simplistic. The examples of sodium and aluminum show immediately that it will bias any calibration for these elements: the more precise *R* values (i.e., those with lower attached uncertainty estimates) obtained for the minerals and rhyolites bias the R_{wm} toward these materials and away from the less precisely measured basalts and andesites.

[77] Table 4 contrasts this approach with three other possibilities for the elements sodium, magnesium and aluminum. The first alternative approach would be to employ the unweighted arithmetic mean R_m for the entire set of GRMs, attaching to it an uncertainty of two standard deviations (95% confidence level); in the general case this would introduce a different, albeit a lesser bias, in favor of whatever subgroups of the GRMs constitute the majority. A second alternative is to take the midpoint of all the measured *R* values and use the extreme values to define the uncertainty. But in either of these two alternatives it is clear that the uncertainty in any so-determined concentration will far exceed the statistical uncertainty inherent in the spectrum fitting procedure. A third alternative is to divide the GRMs into subgroups, and to introduce a different $k(Z)$ factor for each subgroup as the inverse of that subgroup's weighted mean *R* value. If we regard each subgroup as a well-defined population, we can define the uncertainty of its $R_{wm}(Z)$ value through the standard deviation of its mean, generally referred to as EEM or estimated error of the mean [*Bevington and Robinson*, 2003].

[78] The difference between sodium concentrations in a basalt treated by the first and last of these approaches is about 20%, and about 16% for aluminum. Separation into subgroups by igneous rock type, and introduction of the corresponding $k(Z)$ factor into equation (4) thus appears to offer a useful improvement in accuracy. But the obvious drawback of this more refined approach in actual practice is that we do not know a priori which subgroup an unknown rock sample should be assigned to. Several ways out of this impasse exist. If additional experimental information is available it might provide guidance as to the assignment of rock type; Mössbauer or X-ray diffraction data are examples. Another way to assess the rock type is to interrogate the actual APXS data as a first step: the content of salt-forming elements and also the derived CIPW mineral norm [*Rollinson*, 1993] are important hints for the rock type. We would then envisage a two-step process for APXS spectrum analysis. After a preliminary analysis based upon (say) R_m values determined from an entire suite of GRMs, all information on a particular sample would be gathered and an assessment made as to its general rock classification. On the basis of that, a second spectrum fit would be done, this time using a $k(Z)$ function defined specifically from the $R_{wm}(Z)$ value for that classification, e.g., basalts.

[79] In sum, the merit of this two-step approach is that when the rock type can be defined with reasonable confidence, the uncertainties of light element concentrations can be significantly reduced. However, the limitations of the approach must be conceded. In the case of sediments, for example, it may not be useful. The two sediments (MAG-1 and JSD-2) present in the MER APXS calibration suite (with the benefit of hindsight this number is regrettably small) do not show uniform behavior similar to the igneous rock types. For sodium they have *R* values near both the high and low limits of the data, while for magnesium, their *R* values are both situated toward the high extreme.

[80] This two-step approach is an approximation to the suggestion of *Gellert et al.* [2006] that the matrix should be considered, not as an idealized single phase, but as "an assemblage of macroscopically large mineral grains." The matrix terms of equation (4) would then be computed for these specific grains rather than for the average sample composition. The sample surface would be handled as a mixture of different mineral grains, each with its own fractional areal coverage. This more rigorous approach

shares with our present approximation the requirement that information must be available or assumptions need to be made concerning the mineral composition of the sample. The feasibility of this more rigorous approach is under study.

[81] We plan to investigate our two-step approximation suggestion further, using a greatly extended suite of GRMs from an expanded set of suppliers in the context of calibration of the new APXS for the Mars Science Laboratory mission. Additionally, in a forthcoming paper, we will reanalyze the cross-calibration data and a subgroup of the MER data using GUAPX in order to assess the differences, if any, in element concentrations between the present fundamental parameters method and the existing method of *Gellert et al.* [2006].

[82] **Acknowledgments.** Our profound thanks are due to R. G. Rieder, the principal investigator and developer of the APXS during the Pathfinder and MER missions, for the suggestion that we should undertake this work. Similar thanks go to R. Gellert for kindly making available to us the unpublished spectra which he measured using the flight spare MER APXS. The work reported here was supported primarily by the Natural Science and Engineering Research Council of Canada, to which body thanks are expressed by J.L.C. for a Discovery grant and by N.H. and M.L. for NSERC summer scholarships. B.N.J. received partial support from the Canadian Space Agency. Discussions with R. Gellert and P. L. King were, as always, full of insight and extremely helpful; we especially appreciate P. L. King's provision of the TAS diagram. G. Perrett made an important contribution to our understanding of the anorthosite results. We are indebted to B. C. Clark and W. T. Elam for constructive reviews of an early draft and to the journal reviewers for their helpful critiques.

References

Band, I. M., M. B. Trzhaskovskaya, C. W. Nestor Jr., P. O. Tikkanen, and S. Raman (2002), Dirac-Fock internal conversion coefficients, *At. Data Nucl. Data Tables*, *81*, 1–310, doi:10.1006/adnd.2002.0884.

Bernstein, F. (1962), Application of X-ray fluorescence analysis to process control, *Adv. X Ray Anal.*, *5*, 486–499.

Bevington, P. R., and D. K. Robinson (2003), *Data Reduction and Error Analysis for the Physical Sciences*, McGraw-Hill, New York.

Brückner, J., G. Dreibus, R. Gellert, S. Squyres, H. Wänke, A. Yen, and J. Zipfel (2008), Mars Exploration Rovers: Chemical composition by the APXS, in *The Martian Surface*, edited by J. Bell, pp. 58–101, Cambridge Univ. Press, New York.

Campbell, J. L. (2003), Fluorescence yields and Coster-Kronig probabilities for the atomic L subshells, *At. Data Nucl. Data Tables*, *85*, 291–315, doi:10.1016/S0092-640X(03)00059-7.

Campbell, J. L., and G. K. Czamanske (1998), Micro-PIXE in Earth science, *Rev. Econ. Geol.*, *7*, 169–186.

Campbell, J. L., and J.-X. Wang (1991), An improved model for the intensity of low-energy tailing in Si (Li) X-ray spectra, *X Ray Spectrom.*, *20*, 191–197, doi:10.1002/xrs.1300200408.

Campbell, J. L., R. D. Lamb, R. G. Leigh, B. G. Nickel, and J. A. Cookson (1985), Effects of random surface roughness in PIXE analysis of thick targets, *Nucl. Instrum. Methods Phys. Res., Sect. B*, *12*, 402–412, doi:10.1016/0168-583X(85)90040-0.

Campbell, J. L., G. K. Czamanske, L. McDonald, and W. J. Teesdale (1997), Quantitative analysis of major elements in silicate minerals and glasses by micro-PIXE, *Nucl. Instrum. Methods Phys. Res., Sect. B*, *130*, 608–616, doi:10.1016/S0168-583X(97)00258-9.

Claisse, F., and C. Samson (1962), Heterogeneity effects in X-ray analysis, *Adv. X Ray Anal.*, *5*, 335–354.

Firestone, R. B. (1996), *Table of Isotopes*, 8th ed., Wiley-Interscience, New York.

Gellert, R., et al. (2006), Alpha Particle X-ray Spectrometer (APXS): Results from Gusev crater and calibration report, *J. Geophys. Res.*, *111*, E02S05, doi:10.1029/2005JE002555.

Johnston, P. N., and P. A. Burns (1995), Absolute L X-ray intensities in the decays of ^{230}Th, ^{234}U, ^{238}Pu and ^{244}Cm, *Nucl. Instrum. Methods Phys. Res., Sect. A*, *361*, 229–239, doi:10.1016/0168-9002(95)00043-7.

Larkins, F. P. (1971), Dependence of fluorescence yield on atomic configuration, *J. Phys. B At. Mol. Phys.*, *4*, L29–L32, doi:10.1088/0022-3700/4/5/001.

Mallett, C. L., J. M. O'Meara, J. A. Maxwell, and J. L. Campbell (2006), Calibration of the MER α-particle X-ray spectrometer for detection of "invisible" OH and H_2O possibly present in Martian rocks and soils, *X Ray Spectrom.*, *35*, 329–337, doi:10.1002/xrs.914.

Maxwell, J. A., W. J. Teesdale, and J. L. Campbell (1995), The Guelph PIXE software package II, *Nucl. Instrum. Methods Phys. Res., Sect. B*, *95*, 407–421, doi:10.1016/0168-583X(94)00540-0.

Ming, D. W., R. V. Morris, and B. C. Clark (2008), Aqueous alteration on Mars, in *The Martian Surface*, edited by J. Bell, pp. 519–540, Cambridge Univ. Press, New York.

Omand, M., J. A. Maxwell, and J. L. Campbell (2005), Simulation of the relationship between element concentrations and X-ray yields in the Mars Exploration Rover's X-ray Spectrometer, *Nucl. Instrum. Methods Phys. Res., Sect. B*, *229*, 123–136, doi:10.1016/j.nimb.2004.11.014.

Papp, T., and J. L. Campbell (2001), Size and origin of the escape peak in various Si (Li) detectors, *X Ray Spectrom.*, *30*, 77–82, doi:10.1002/xrs.459.

Potts, P. J. (1987), *A Handbook of Silicate Rock Analysis*, Blackie, Glasgow, U.K.

Rieder, R., H. Wänke, T. Economou, and A. Turkevich (1997), Determination of the chemical composition of Martian soil and rocks: The alpha proton X-ray spectrometer, *J. Geophys. Res.*, *102*, 4027–4044, doi:10.1029/96JE03918.

Rieder, R., R. Gellert, J. Brückner, G. Klingelhöfer, G. Dreibus, A. Yen, and S. W. Squyres (2003), The new Athena Alpha Particle X-ray Spectrometer for the Mars Exploration Rovers, *J. Geophys. Res.*, *108*(E12), 8066, doi:10.1029/2003JE002150.

Rollinson, H. (1993), *Using Geochemical Data: Evaluation, Presentation, Interpretation*, Pearson, Harlow, U. K.

Van Grieken, R., and A. Markowicz (2002), *Handbook of X-ray Spectrometry*, Marcel Dekker, New York.

S. M. Andrushenko, J. L. Campbell, N. G. Holmes, M. Lee, J. A. Maxwell, and S. M. Taylor, Guelph-Waterloo Physics Institute, University of Guelph, Guelph, ON N1G 2W1, Canada. (jlc@physics.uoguelph.ca)

B. N. Jones, Surrey Ion Beam Centre, University of Surrey, Guildford GU2 7XH, U.K.